LUND UNIVERSITY

FACULTY OF SCIENCE

An Elevated N_2-to-NO Transition Temperature in Ammonia Oxidation on Polycrystalline Palladium

A Pulsed Time-Resolved Ambient-Pressure XPS Study

Hong-Ye Lin

Thesis submitted for the degree of Master of Science

Project duration: 9 months (60ECTS)

Supervisor: Jan Knudsen, Co-Supervisor: Ulrike Küst

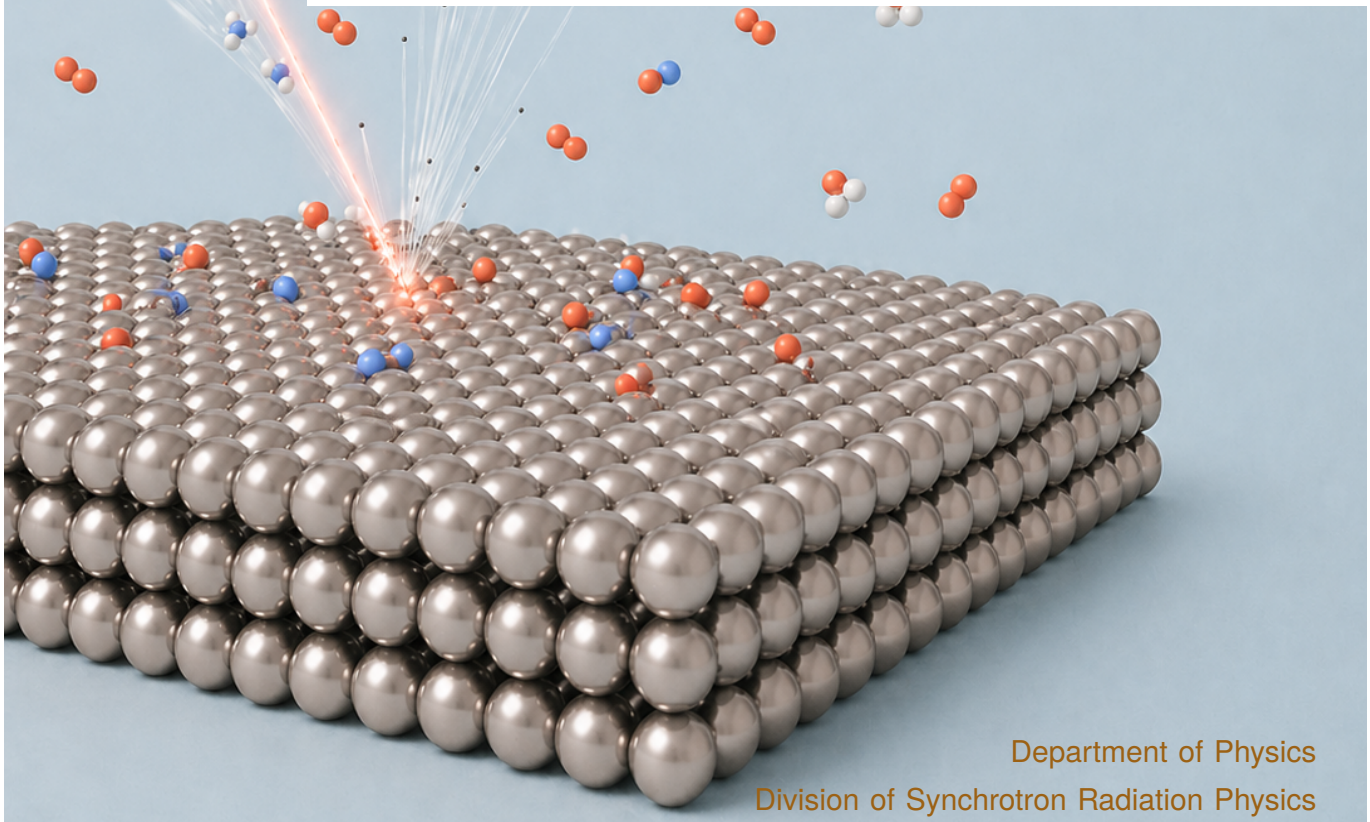

Department of Physics

Division of Synchrotron Radiation Physics

May 2026

Abstract

Catalytic oxidation of ammonia (NH_3) is the key reaction in the Ostwald process for industrial nitric acid production. The reaction yields three nitrogen-containing products, N_2, N_2O, and NO, and the selectivity between them depends on the catalyst and the operating conditions. Most of what is known comes from steady-state studies on platinum and rhodium. This thesis studies what happens when the reactant supply is varied over time rather than held constant.

Time-resolved ambient-pressure X-ray photoelectron spectroscopy (tr-APXPS) is used to follow NH_3 oxidation on a polycrystalline palladium catalyst at 500°C and 600°C. The catalyst is held under a 1 mbar O_2 flow, and short NH_3 pulses are repeatedly injected over 120 cycles to enable event-averaging.

Three findings emerge. First, the Pd surface composition differs sharply between the two temperatures, dominated by Pd oxide at 500°C and largely metallic at 600°C. Second, the product selectivity shifts toward NO at the higher temperature, in the same direction as the Pt/Rh literature. Third, the NH_3 conversion drops from 94% to 80% with increasing temperature, while the peak oxygen conversion stays around 40% at both temperatures.

We propose that the conversion drop reflects the temperature-driven change in surface O coverage: by analogy with DFT results reported on Pt, adsorbed O and OH species at 500°C may assist NH_3 dehydrogenation more than the metallic surface at 600°C. The transition to NO-dominated selectivity also occurs at a higher temperature than reported for steady-state Pt/Rh (below 600 K), with N_2 and N_2O still accounting for nearly half of the products at 500°C. Two factors may contribute: the catalyst (Pd rather than Pt or Rh, possibly with longer surface N residence) and the pulsed delivery, which may briefly raise the surface N coverage.

Abbreviations

APXPS	Ambient-Pressure X-ray Photoelectron Spectroscopy
BE	Binding Energy
DFT	Density Functional Theory
DLD	Delay-Line Detector
ESCA	Electron Spectroscopy for Chemical Analysis
FTIR	Fourier Transform Infrared
IMFP	Inelastic Mean Free Path
KE	Kinetic Energy
MES	Modulation Excitation Spectroscopy
sccm	Standard Cubic Centimeters per Minute
TPD	Temperature-Programmed Desorption
tr-APXPS	Time-Resolved Ambient-Pressure X-ray Photoelectron Spectroscopy
UHV	Ultra-High Vacuum
XPS	X-ray Photoelectron Spectroscopy

Contents

1 Introduction

Synthetic nitrogen fertilizer feeds roughly half of the world today. A century ago, this share was essentially zero [1]. Two catalytic processes invented in the early twentieth century drive this growth. The Haber-Bosch process combines atmospheric N_2 and H_2 over an iron catalyst to produce ammonia (NH_3). The Ostwald process then converts that ammonia over a platinum-rhodium gauze at $\sim 900°C$ to nitric oxide (NO), the precursor to nitric acid (HNO_3) and synthetic fertilizer [2]. This thesis focuses on the second step: the catalytic oxidation of NH_3.

NH_3 oxidation can yield three nitrogen-containing products, N_2, N_2O, and NO. The proportion in which they are formed is called the selectivity of the reaction. The selectivity depends on the catalyst surface and on the operating conditions, including temperature, pressure, and the NH_3:O_2 ratio. In this thesis we focus on the role of temperature. Across previous studies on Pt and Rh, the selectivity shifts with temperature: lower temperatures favor N_2 and N_2O, while higher temperatures favor NO [2]. The Ostwald process is operated at high temperature in part for this reason, since any NH_3 that becomes N_2 or N_2O is lost from the NO yield.

To understand why higher temperature favors NO formation, much of what is known about NH_3 oxidation selectivity comes from simplified model systems based on pure Pt, Rh, or PtRh alloys, often on single crystals. On Pt and Rh, the selectivity shifts with temperature, with N_2 dominating at lower temperatures and NO at higher temperatures, and the transition below 600 K depending on the catalyst and the gas composition [2, 3]. The literature interprets this within a surface-coverage picture: surfaces rich in NH_x and atomic N favor N_2, those rich in O favor NO, and mixtures of N and NO produce N_2O [4, 5]. This is developed further in Section 2.1.1.

All of these observations come from steady-state experiments, in which the catalyst surface reaches a common equilibrium with the gas. In this thesis, we ask what happens when the reactant supply is varied over time rather than held constant. The catalyst is kept under a steady O_2 flow that maintains an O-rich surface, and NH_3 is introduced as a short pulse. The pulsed delivery drives the surface through transient configurations that do not form at equilibrium, and the time-resolved measurement follows both the surface and the gas-phase products through the pulse.

The pulsed approach calls for a technique with three properties. It must be surface-sensitive, because the catalytic reaction takes place on the topmost atomic layers of the catalyst. It must be operando, so that the measurement is made while the reaction is running. And it must be time-resolved, so that the surface can be followed during the NH_3 pulse. Time-resolved ambient-pressure X-ray photoelectron spectroscopy (tr-APXPS) is the technique that meets all three.

Time resolution is a further concern. To follow the reaction dynamically, a short acquisition time on the order of 0.1 s is needed, but within such a short window too few photoelectrons are collected for meaningful analysis. The usual remedy is to extend the acquisition time,

which improves the spectral quality but sacrifices the time resolution. If a catalytic reaction is reproducible, Knudsen et al. [6] and Eads et al. [7] showed that this trade-off can be avoided by repeating the same gas pulse over many cycles and defining a common reference event in each cycle, for example, the electronic trigger that opens the gas pulse valve, so that snapshots taken at equivalent times after this reference can be aligned across cycles and averaged. The quality of each short-time spectrum is thereby improved without sacrificing time resolution. This technique is called event-averaging.

Building on this pulsed tr-APXPS setup, the experiment is carried out on a Pd polycrystal. Pd is chosen because it readily forms a surface oxide at mbar pressures and cycles between metallic and oxide states with temperature, while keeping catalytic properties similar to Pt. The catalyst is held under an O_2 flow in the mbar regime, and short NH_3 pulses are injected into this flow. The same pulse is repeated 120 times so that event-averaging can be applied.

Three findings emerge from these pulsed measurements. First, the Pd surface shows distinctly different phases at the two temperatures. At 500°C the surface is dominated by Pd oxide, whereas at 600°C the oxide is much reduced and the surface is largely metallic Pd. Second, the product selectivity shifts with temperature, with NO dominating at the higher temperature and N_2 and N_2O appearing at the lower temperature. We propose that this shift follows from a shorter surface N residence time at higher temperature. Third, the NH_3 conversion drops from 94% at 500°C to 80% at 600°C, while the peak oxygen conversion is similar at both temperatures, around 40% of the available oxygen.

The selectivity shift goes in the same direction as the literature, since higher temperature favors NO. However, the transition occurs at a higher temperature in our experiment than in steady-state studies on Pt and Rh, which report transitions below 600 K. At 500°C, well above this range, our measurement still shows substantial N_2 and N_2O production. Two factors may contribute to this elevated N_2 and N_2O production: the catalyst itself (Pd rather than Pt or Rh, with possibly longer surface N residence in the framework of Ivashenko et al. [5]) and the pulsed delivery, which may briefly raise the surface N coverage during each pulse. The two contributions cannot be separated from our two-temperature dataset.

The NH_3 conversion drop is unexpected from an Arrhenius perspective, since higher temperature normally accelerates the reaction. We propose that it reflects the temperature-driven change in surface O coverage: by analogy with DFT results reported on Pt [2], adsorbed O and OH species at 500°C may assist NH_3 dehydrogenation more than the metallic surface at 600°C (Section 4.4.3).

2 Theory

2.1 Catalysis

A catalyst is a substance that increases the rate of a chemical reaction without being consumed in the process. In heterogeneous catalysis, the catalyst and the reactants are in different phases. In this thesis, gaseous NH_3 and O_2 react on a solid palladium catalyst surface.

When a gas molecule approaches the surface, it can chemisorb. The molecule then forms a chemical bond with the surface atoms through the overlap of their electron orbitals. Chemisorbed molecules are adsorbed at specific sites on the surface, where the local electronic structure and geometry of the surface atoms make this an energetically favorable bonding site. The preferred adsorption site depends on the surface structure, temperature, and pressure [8].

The key function of a catalyst is to lower the activation energy E_a of a reaction. Without a catalyst, the reactants must overcome a large energy barrier to form products. The catalyst provides an alternative reaction pathway with a lower barrier, often by breaking the reaction into several intermediate steps on the surface. The relationship between the reaction rate constant k and temperature T is described by the Arrhenius equation:

$$k = A \times e^{-\frac{E_a}{k_B T}} \tag{1}$$

where A is the pre-exponential factor and k_B is the Boltzmann constant. A lower E_a leads to a higher reaction rate at a given temperature.

A heterogeneous catalytic reaction generally proceeds in three stages, as illustrated in Figure 1 for the case of NH_3 oxidation. First, the reactant molecules adsorb onto the catalyst surface. Second, the adsorbed molecules dissociate and the resulting fragments diffuse across the surface. Third, the fragments recombine to form product molecules, which then desorb from the surface. The catalyst itself remains unchanged after the reaction cycle and is available for the next cycle [8].

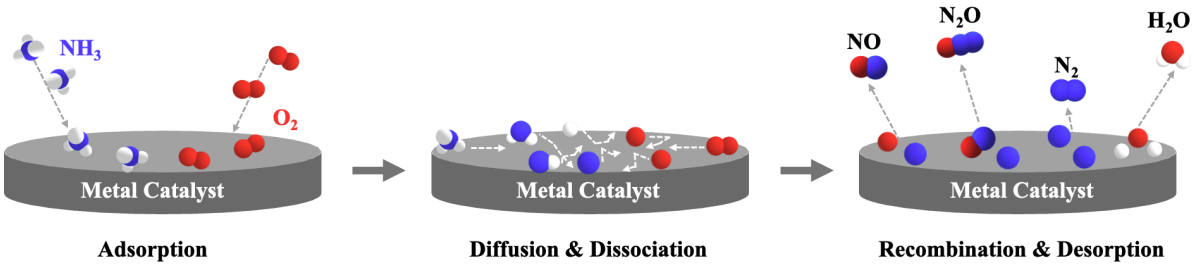

Figure 1: Schematic illustration of the three stages of a heterogeneous catalytic reaction for the case of NH_3 oxidation.

2.1.1 NH_3 Oxidation on Metal Surfaces

The catalytic oxidation of ammonia can produce several different products depending on the reaction conditions. The formation of N_2, N_2O, and NO is described by the following reactions:

$$4\,NH_3 + 3\,O_2 \longrightarrow 6\,H_2O + 2\,N_2 \tag{2}$$

$$4\,NH_3 + 4\,O_2 \longrightarrow 6\,H_2O + 2\,N_2O \tag{3}$$

$$4\,NH_3 + 5\,O_2 \longrightarrow 6\,H_2O + 4\,NO \tag{4}$$

The selectivity of the reaction, meaning which product is preferentially formed, depends on factors such as the temperature and the surface state of the catalyst. Understanding and controlling this selectivity is important both for industrial and environmental applications. In the Ostwald process, for example, NH_3 is oxidized over a platinum-rhodium gauze catalyst at high temperatures to selectively produce NO, which is a precursor for the synthesis of nitric acid [2].

On the catalyst surface, both O_2 and NH_3 are adsorbed and decomposed into atomic O, N, and H. These atoms then recombine on the surface to form the reaction products. At the high temperatures relevant for catalytic NH_3 oxidation, hydrogen atoms react with surface oxygen to form H_2O rather than recombining into H_2 [5]. This explains why H_2O appears as a common byproduct in all three overall reactions. The general process follows the three catalytic stages described in Section 2.1 and illustrated in Figure 1.

On platinum surfaces, the decomposition of NH_3 has been studied in more detail. Weststrate et al. [4] observed the stepwise dehydrogenation $NH_3 \rightarrow NH_2 \rightarrow NH \rightarrow N$ on Pt(410) using XPS, by identifying the corresponding N 1s spectral components at different temperatures. Density functional theory (DFT) calculations by Baerns et al. [2] further show that on Pt, adsorbed O and OH significantly lower the activation barriers for each dehydrogenation step, with the released hydrogen contributing to H_2O formation. Although this detailed pathway has only been established on Pt, Pd shares similar electronic and catalytic properties, and a similar decomposition process may apply.

After decomposition, the atomic nitrogen remaining on the surface can follow several pathways. Two neighboring N atoms can recombine to form N_2. Alternatively, N can react with adsorbed O to form NO. A third pathway involves the reaction of N with adsorbed NO to produce N_2O. Which pathway is followed depends on the relative populations of N- and O-containing species on the surface.

In UHV studies on Pt(410), Weststrate et al. [4] used temperature-programmed desorption (TPD) and synchrotron XPS at 10^{-7} mbar partial pressures and an NH_3:O_2 ratio of 1:5. They showed that surfaces dominated by NH_x and atomic N favor N_2, O-covered surfaces favor NO, and N_2O forms only when adsorbed N and NO coexist. Baerns et al. [2] extended this work to higher pressures, reviewing Pt(533), Pt foil, and Pt gauze across 10^{-5} mbar to 1 bar, with N_2

favored below ~600 K and NO above, and higher O_2/NH_3 ratios shifting the transition to lower temperatures. The above studies focus on the role of temperature.

The effect of gas composition has been examined separately. Rafti et al. [3] observed on Rh(110) that a large oxygen excess (O_2:NH_3 = 10:1) strongly suppressed N_2 production and reduced the overall catalytic activity. Ivashenko et al. [5], in an operando APXPS study on Pt(111) and PtRh/Pt(111) surfaces, argued that N_2 formation requires a sufficient surface N coverage. Below this threshold, atomic N predominantly reacts with O to form NO.

2.1.2 The Pd Polycrystal Catalyst

Surface science studies of catalytic reactions are most often carried out on single crystals, where one well-defined surface orientation is exposed [8]. The atomic arrangement is then periodic, which lets the surface structure be measured cleanly.

However, real catalyst particles are more complex. They expose many orientations at once, along with grain boundaries and defects that a single crystal does not reproduce. A polycrystal narrows this gap. Polished polycrystals are smooth enough for surface analysis while still presenting a range of orientations at the same time, closer to a real working catalyst. The catalyst used in this thesis is a polycrystalline palladium (Pd) sample, previously used in our group for catalytic methane oxidation [9], so the surface preparation and behavior are well characterized.

The choice of Pd is motivated by its surface chemistry under the conditions of this work. At mbar pressures, Pd readily forms a surface oxide and cycles between metallic and oxide states as the temperature is varied, which is a central observation of this thesis. Pt, by contrast, does not easily form an oxide at mbar pressures, and Pd otherwise has catalytic properties similar to Pt, making it a relevant model system. NH_3 oxidation on polycrystalline Pd has been less studied than on Pt or Rh, which adds fundamental interest. In our measurement, the X-ray beam spot is larger than the average grain size of the Pd polycrystal, so the spectra reflect an average over many orientations rather than any individual one.

2.2 Photoelectron Spectroscopy

Heterogeneous catalysis takes place at the interface between the solid catalyst and the gas, so the chemistry of interest is concentrated in the topmost atomic layers. Probing this region requires a technique that provides chemical and electronic information from the surface alone. Photoelectron spectroscopy meets this need.

Photoelectron spectroscopy is surface-sensitive because the inelastic mean free path (IMFP) of an electron in a solid is short, only several atomic layers (5–10 Å) over the energy range relevant for XPS. The IMFP depends on the electron kinetic energy (KE) and is shown in Figure 2. Only photoelectrons emitted from the topmost atomic layers therefore escape without inelastic scattering, while those from deeper regions lose chemical information. Electrons are

also straightforward to detect, count, and steer by external fields, which makes the technique experimentally practical.

Photoemission was first observed by Heinrich Hertz in 1887. In 1905, Albert Einstein explained that the emitted electrons are excited by photons, an interpretation now known as the photoelectric effect, for which he received the Nobel Prize in Physics in 1921 [10]. In the 1960s, Kai Siegbahn developed X-ray photoelectron spectroscopy (XPS), originally named electron spectroscopy for chemical analysis (ESCA), and was awarded the Nobel Prize in Physics in 1981 for this work [11]. XPS is the technique used in this thesis.

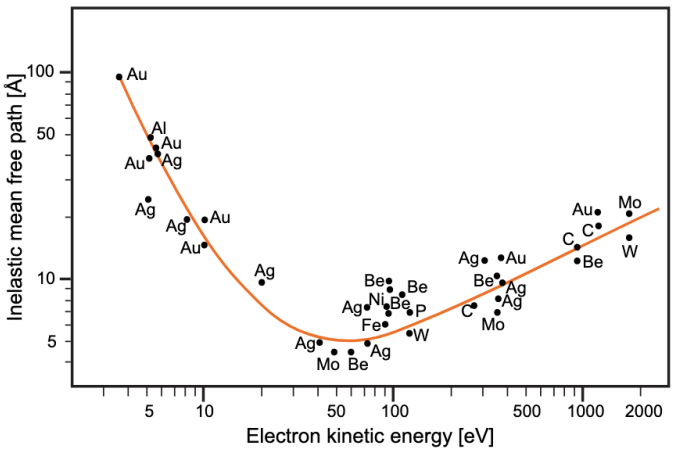

Figure 2: Inelastic mean free path (IMFP) of electrons as a function of kinetic energy. Figure taken from [12].

2.3 X-ray Sources

The synchrotron radiation source used in this thesis provides tunable, intense X-rays for photoelectron spectroscopy. In a synchrotron facility, electrons are first accelerated to a speed close to the speed of light before being injected into the storage ring. As these relativistic electrons pass through insertion devices such as undulators, they emit intense electromagnetic radiation. By adjusting the magnetic array (for instance, altering the undulator gap), the emitted photon energy can be precisely tuned. This tunability lets us choose $h\nu$ such that the photoelectron kinetic energy from a given core level falls in the 100–300 eV range, where the inelastic mean free path is shortest (Figure 2) and the measurement is most surface-sensitive.

This thesis project's experiments were mainly conducted at the MAX IV Laboratory HIPPIE beamline. The HIPPIE beamline is located at the 3 GeV ring and provides a tunable photon energy range between 250 eV and 2200 eV [13].

2.4 Ambient-Pressure Electron Analyzer

A challenge for XPS at ambient pressure is that the photoelectrons must travel from a sample in the mbar gas environment to a detector under ultra-high vacuum (UHV), which is required both to avoid inelastic scattering of the electrons by gas molecules and to protect the detector. To overcome this, Ogletree et al. [14] introduced a differentially pumped electrostatic lens system that links the high-pressure sample region to the UHV analyzer, making XPS at mbar pressures accessible. This is the type of analyzer used in this thesis, shown schematically in Figure 3.

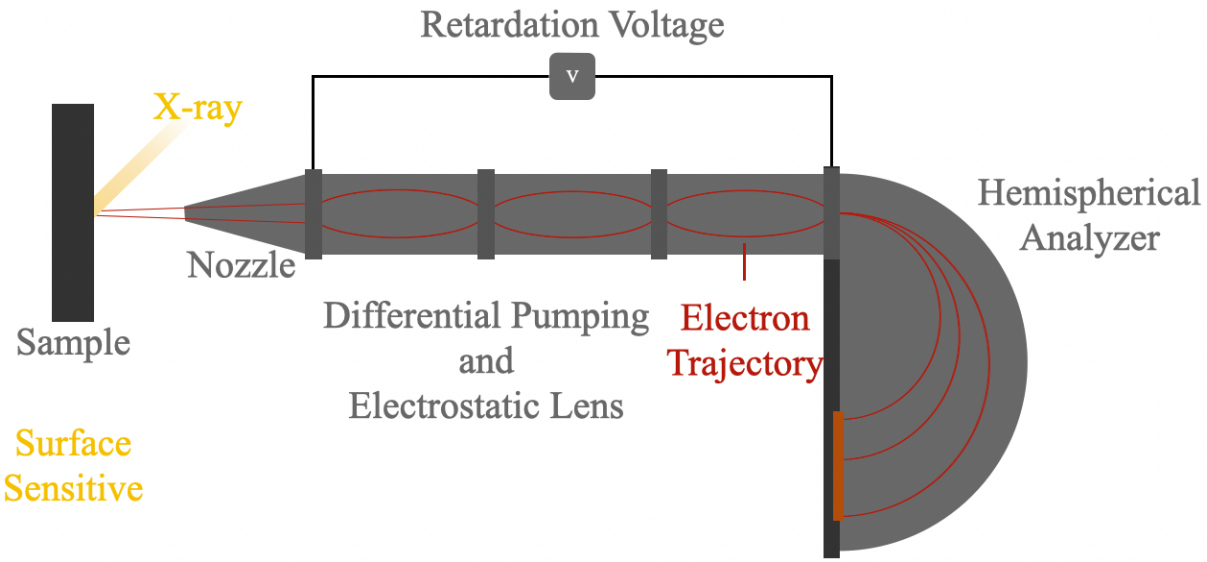

Figure 3: Schematic of a differentially pumped hemispherical analyzer with electrostatic lenses for ambient-pressure XPS. Figure adapted from [14].

After emission from the sample, the photoelectron enters the nozzle together with surrounding gas molecules. Electrostatic lenses focus photoelectrons emitted over a larger solid angle into the nozzle, increasing the number of electrons that reach the analyzer. The differential pumping stages between the nozzle and the analyzer progressively reduce the gas pressure, so the photoelectron arrives at the analyzer in vacuum without significant inelastic scattering.

Inside the analyzer, the photoelectron first passes a retardation stage where its kinetic energy is adjusted by an applied voltage. Only electrons with a specific kinetic energy, the pass energy, follow the correct trajectory through the hemispherical region and reach the detector. By varying the retardation voltage, the analyzer scans the photoelectron spectrum at different binding energies. The pass energy is typically set to 50, 100, or 200 eV.

The electron finally arrives at a delay-line detector (DLD), shown together with the hemispherical analyzer in Figure 4. The DLD records the two-dimensional position of each photoelectron impact through two orthogonal meander-structured wires in the X (orange) and Y (gray) directions. When an electron hits the detector, it induces electrical pulses that propagate in opposite directions along each delay line, denoted I_{x1} and I_{x2} along X, and I_{y1} and I_{y2} along Y. The pulses arrive at the ends of each line with a time difference, and the impact position along

that direction is calculated from this delay. The X-coordinate of the impact corresponds to the photoelectron kinetic energy, while the Y-coordinate is the non-energy-dispersive direction. In this thesis, only the X-coordinate is used in the analysis.

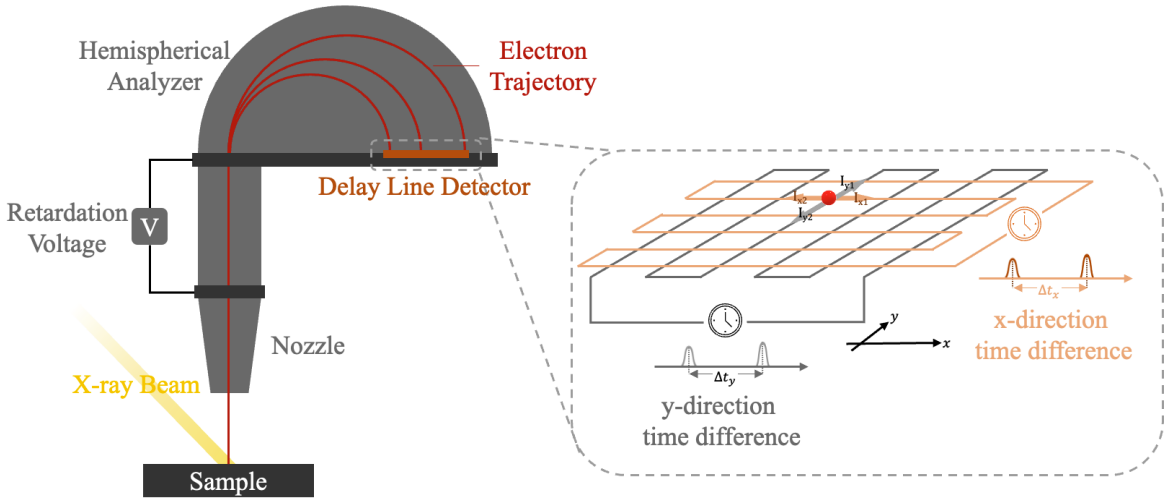

Figure 4: Schematic of the hemispherical analyzer and delay-line detector (DLD) used for measuring photoelectrons.

2.5 Binding Energy in Solids and Gases

In this work, X-rays excite core-level electrons from two sources: the solid catalyst surfaces (Pd and adsorbed species) and gas-phase molecules (NH_3, O_2, and H_2O) near the surface.

Figure 5 shows the relevant energy diagram. The vertical axis is energy; the horizontal axis is spatial position, covering the solid, gas, and analyzer regions. The solid sample and the analyzer are held at the same ground potential, so their Fermi levels ($E^{\text{Solid}}_{\text{Fermi}}$ and $E^{\text{Analyzer}}_{\text{Fermi}}$) are aligned. The vacuum level in the solid and analyzer region, $E^{\text{Solid}}_{\text{Vacuum}}$ and $E^{\text{Analyzer}}_{\text{Vacuum}}$, each lie above their Fermi level by the corresponding work function, ϕ_{Solid} and ϕ_{Analyzer}. As the gas phase is positioned between the conductive sample and analyzer nozzle, $E^{\text{Gas}}_{\text{Vacuum}}$ varies linearly between them, from $E^{\text{Solid}}_{\text{Vacuum}}$ at the solid surface to $E^{\text{Analyzer}}_{\text{Vacuum}}$ at the analyzer. The core levels $E^{\text{Solid}}_{\text{core}}$ and $E^{\text{Gas}}_{\text{core}}$, for example, Pd $3p_{3/2}$ or O 1s, lie below the corresponding Fermi or vacuum level. Because the binding energy of a core electron in a gas-phase molecule is set by the molecule's internal structure and does not depend on the local electrostatic environment, $E^{\text{Gas}}_{\text{core}}$ stays at a fixed offset below $E^{\text{Gas}}_{\text{Vacuum}}$ everywhere in the gas region. The two levels therefore remain parallel as $E^{\text{Gas}}_{\text{Vacuum}}$ varies linearly across the gas region. In Figure 5, the yellow circles represent electrons and the blue arrows show their excitation by a photon of energy $h\nu$.

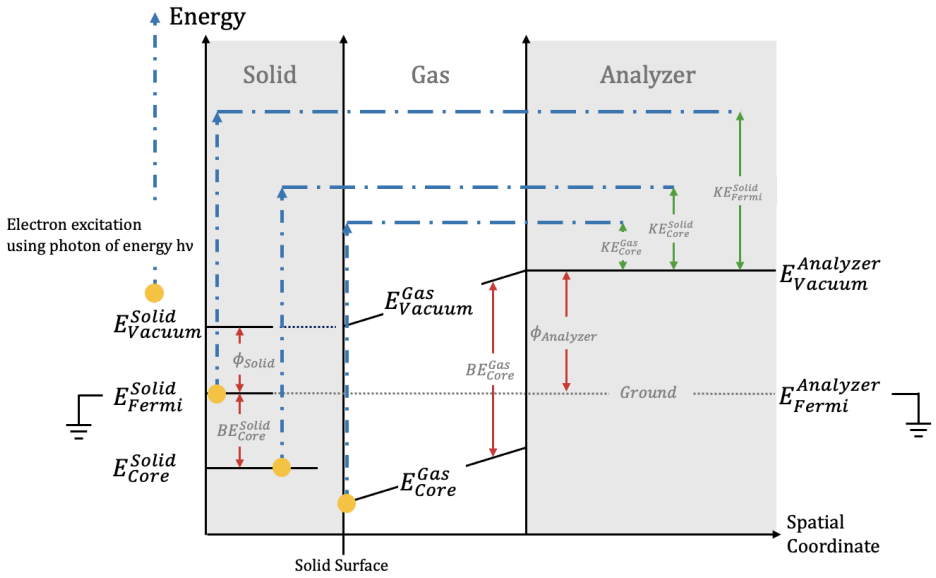

Figure 5: Energy level alignment between solid, gas, and analyzer during the photoemission process.

In XPS, core-level energies are reported as binding energies, defined as the energy of a core electron relative to a reference level. The choice of reference differs between solid and gas because of how each is electrically connected to the analyzer. The solid sample is in electrical contact with the analyzer, so their Fermi levels align. This shared level serves as the reference for the solid, and the solid-phase binding energy $BE^{\text{Solid}}_{\text{Core}}$ is the gap between $E^{\text{Solid}}_{\text{Fermi}}$ and $E^{\text{Solid}}_{\text{core}}$. Gas-phase molecules near the surface are electrically isolated from the analyzer, so no such shared reference exists. Their binding energy is instead referenced to the local vacuum level: $BE^{\text{Gas}}_{\text{Core}}$ is the gap between $E^{\text{Gas}}_{\text{Vacuum}}$ and $E^{\text{Gas}}_{\text{core}}$.

The analyzer detects three kinds of photoelectrons: the core level of the gas near the surface, and the core level and Fermi level of the solid, with energies $KE^{\text{Gas}}_{\text{Core}}$, $KE^{\text{Solid}}_{\text{Core}}$, and $KE^{\text{Solid}}_{\text{Fermi}}$. Reading directly from the diagram, for the solid:

$$KE^{\text{Solid}}_{\text{Core}} = h\nu - (BE^{\text{Solid}}_{\text{Core}} + \phi_{\text{Analyzer}}) \tag{5}$$

$$KE^{\text{Solid}}_{\text{Fermi}} = h\nu - \phi_{\text{Analyzer}} \tag{6}$$

Subtracting Eq. (5) from Eq. (6):

$$BE^{\text{Solid}}_{\text{Core}} = KE^{\text{Solid}}_{\text{Fermi}} - KE^{\text{Solid}}_{\text{Core}} \tag{7}$$

Therefore, $BE^{\text{Solid}}_{\text{Core}}$ is independent of both $h\nu$ and ϕ_{Analyzer}, which makes it directly comparable across experimental setups.

Reading similarly from the diagram, for a gas-phase molecule near the solid surface:

$$KE^{\text{Gas}}_{\text{Core}} = h\nu - (BE^{\text{Gas}}_{\text{Core}} + (\phi_{\text{Analyzer}} - \phi_{\text{Solid}})) \tag{8}$$

Compared to Eq. (5), ϕ_{Analyzer} is replaced by the $(\phi_{\text{Analyzer}} - \phi_{\text{Solid}})$ term. This is because $KE^{\text{Gas}}_{\text{Core}}$ is referenced to $E^{\text{Gas}}_{\text{Vacuum}}$ rather than the shared Fermi level, and near the surface $E^{\text{Gas}}_{\text{Vacuum}}$ lies ϕ_{Solid} above it.

Subtracting Eq. (8) from Eq. (6) eliminates $h\nu$ and ϕ_{Analyzer}:

$$BE^{\text{Gas}}_{\text{Core}} - \phi_{\text{Solid}} = KE^{\text{Solid}}_{\text{Fermi}} - KE^{\text{Gas}}_{\text{Core}} \tag{9}$$

The left-hand side of Eq. (9) is the measured binding energy of a gas-phase peak, offset from its intrinsic value $BE^{\text{Gas}}_{\text{Core}}$ by $-\phi_{\text{Solid}}$. When ϕ_{Solid} changes, the observed gas-phase peak shifts accordingly [15]. Section 3.3 describes how $KE^{\text{Solid}}_{\text{Fermi}}$ is measured and used in Eq. (7) to obtain binding energies from every snapshot spectrum.

2.6 Chemical Shift

The kinetic energy of a photoelectron depends not only on which atom and orbital it comes from, but also on the local chemical environment. The same core level therefore appears at slightly different binding energies in different chemical compounds, an effect known as the chemical shift.

As an example, consider the N 1s level in ammonia (NH_3) and nitric oxide (NO). Both contain a single nitrogen atom, but the bonding partners differ in electronegativity. In NH_3, nitrogen is bonded to three hydrogen atoms. Because hydrogen is less electronegative than nitrogen, the valence electrons stay close to the nitrogen and shield the N 1s electrons from the nuclear charge. In NO, nitrogen is bonded to a more electronegative oxygen atom, and the valence electrons are drawn toward oxygen, reducing the shielding. The N 1s electrons in NO therefore experience a stronger effective nuclear charge, leading to a higher binding energy than in NH_3. This shift is directly observable in the gas-phase N 1s spectra of this thesis (Section 4).

2.7 Modulation Excitation Spectroscopy

As discussed in Section 2.4, ambient pressure XPS operates at mbar-range pressures where photoelectrons undergo significant scattering by gas molecules. Combined with the low photoionization cross-section, that is, the low probability of generating a photoelectron from a given atom, the number of detected photoelectrons per unit time is small. When high time resolution is required, for example, to follow a catalytic reaction with sub-second time steps, the acquisition time per spectrum becomes very short, and the resulting spectra are dominated by noise. This makes detailed analysis such as peak fitting unreliable or even impossible for individual time-resolved spectra.

Modulation excitation spectroscopy (MES) provides a way to recover signal quality without sacrificing time resolution. The central idea, introduced by Baurecht and Fringeli [16] in the context of Fourier-transform infrared (FTIR) spectroscopy, is to periodically modulate

an external parameter (such as temperature, pressure, or gas composition) and measure the spectroscopic response over many repeated cycles. Because the modulation is periodic, the response of any species affected by the perturbation is also periodic. The key assumption is that each cycle is reproducible: the system returns to the same starting condition and undergoes the same process. Noise can be suppressed by averaging across cycles. Contributions from inactive species can be separated from the active response through demodulation techniques such as Fourier analysis [9].

Knudsen et al. [6] applied this averaging approach to operando APXPS at the HIPPIE beamline (MAX IV), and Eads et al. [7] subsequently extended it to the microsecond regime on the same beamline. In their approach, a catalyst surface is repeatedly exposed to the same gas pulse sequence while XP spectra are recorded continuously. Spectra collected at the same relative time point within different cycles correspond to the same surface state and can be averaged together. This procedure, called event-averaging, improves the signal-to-noise ratio in proportion to $\sqrt{N}$, where N is the number of averaged cycles. With this method, high-quality time-resolved APXPS data with sub-second resolution become accessible even under conditions where individual spectra are too noisy for any meaningful analysis.

In this thesis, the modulation parameter is the gas-phase composition. The Pd catalyst is kept under a constant O_2 flow at 1 mbar, and a short NH_3 pulse (0.5 s duration, 1 sccm) is injected every 10 seconds. This periodic pulse sequence is repeated for 120 cycles, providing sufficient statistics for event-averaging. The detailed implementation (how the modulation period is determined and how spectra from different cycles are aligned and averaged) is described in the Data Treatment section (Section 3.5).

Beyond the improvement in signal quality, the pulsed experimental design also offers a scientific advantage. Because each cycle starts from a well-defined, oxygen-covered Pd surface with no nitrogen present, the arriving NH_3 pulse drives the surface through a sequence of transient states: from oxygen-rich, through a reduction phase where surface oxygen is consumed, and back to the oxygen-covered state as the system recovers. These transient surface states (for example, a temporarily reduced Pd surface at 500°C) would not form under steady-state co-feed conditions. In a steady-state experiment, the surface reaches an equilibrium between oxygen adsorption, NH_3 dissociation, and product desorption. This balance does not change with time as long as the gas composition remains constant. The pulsed experiment forces the surface away from this balance and drives it through states that only exist for a short time. By combining this pulsed design with event-averaging, we can capture these short-lived states with sufficient spectral quality for quantitative analysis. The simultaneous probing of the gas phase further means that the catalytic activity associated with each transient surface state can also be measured.

3 Data Treatment

3.1 Spectrum Acquisition Modes and Transmission Function Correction

XP spectra can be acquired in two modes. In swept mode, the hemispherical analyzer sweeps through a range of kinetic energies by gradually changing the retardation voltage. Because the retardation voltage is scanned, electrons of the same kinetic energy hit different positions along the energy-dispersive direction of the detector during the scan. This averages out the non-uniform detection efficiency. The swept spectrum therefore provides the true relative intensities. However, the acquisition time is approximately 10–30 seconds. Since catalytic reactions can occur on timescales of 100 ms or faster, swept mode cannot capture these dynamics.

In snapshot mode, the retardation voltage is fixed, and the detector records all photoelectrons within its energy window simultaneously. The time resolution is set by the photoelectron count rate. The delay-line detector time-stamps each event with picosecond precision, so the detector itself does not impose a meaningful limit. In our experiment, the practical time resolution is on the order of 0.1 s per snapshot, set by how many photoelectrons accumulate within that window. This makes snapshot mode the standard choice for time-resolved measurements. The drawback of snapshot mode is that the relative peak intensities are distorted, for two reasons. First, the detection efficiency of the 2D delay-line detector is not homogeneous, so different positions on the detector record electrons with different efficiencies. Second, the analyzer transmits different kinetic energies with different efficiencies. The transmission function below corrects for both.

To correct this distortion, a transmission function is determined by measuring a snapshot and a swept spectrum under the same conditions:

$$T(E) = \frac{I_{\text{swept}}(E)}{I_{\text{snap}}(E)} \tag{10}$$

where $I_{\text{swept}}(E)$ and $I_{\text{snap}}(E)$ are the swept and snapshot intensities at binding energy E, both time-averaged over their acquisition windows. The calibration is performed on a chemically stable sample. Each snapshot spectrum is then multiplied by $T(E)$ to obtain the correct relative intensities. Figure 6 illustrates this using the O 1s surface spectra. The snapshot (orange) and swept (blue) spectra are plotted on the left y-axis. The two spectra have clearly different shapes. For example, the peak near 530 eV is much stronger in the snapshot spectrum than in the swept spectrum. The transmission function (green, right y-axis) captures this difference: at low binding energy, $T(E)$ drops below 1, meaning the snapshot overestimates the intensity in this region. After multiplying by $T(E)$, the corrected snapshot spectrum will have the same shape as the swept spectrum. This transmission function is measured once and then applied to every time-resolved snapshot spectrum acquired in the same binding energy region.

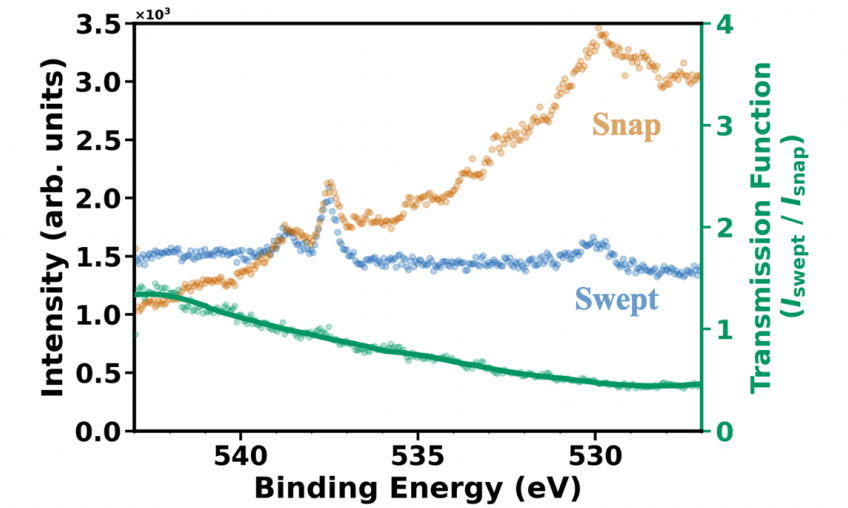

Figure 6: Comparison of snapshot and swept O 1s surface spectra to determine the transmission function $T(E)$ for intensity correction.

3.2 Attenuation Normalization

After the transmission function correction, the relative intensities within each snapshot spectrum match those of a swept spectrum. The total intensity, however, can still vary between snapshots taken at different time points. Two non-chemical sources contribute to this artificial variation. During the NH_3 pulse, the gas density between the sample and the analyzer nozzle temporarily rises, attenuating the photoelectron flux through inelastic scattering. The X-ray flux delivered to the sample also fluctuates slightly with time, on a slower timescale. Both effects modulate the total count rate without carrying chemical information, and have to be removed before snapshots at different time points can be compared directly.

The correction uses the secondary-electron background that fills the region between core-level peaks. The background intensity is proportional to the X-ray flux and to the number of photoelectrons that travel through the gas phase to the detector, so it tracks both sources of artificial variation simultaneously. For each snapshot, the median intensity in a binding energy region that contains no photoemission peak is used as the divisor. After this step, the baseline is set to one for every spectrum, and the chemical content of each peak can be compared directly across time.

3.3 Fermi Edge Calibration

At a synchrotron, the photon energy is set manually to a chosen nominal value, but the actual delivered value can deviate slightly. From Eq. (6) in Section 2.5, an electron at the Fermi edge has kinetic energy $KE^{\text{Solid}}_{\text{Fermi}} = h\nu - \phi_{\text{Analyzer}}$, so the Fermi edge should appear at $BE = 0$ if $h\nu$ matches its nominal value. Any deviation of the measured Fermi edge from $BE = 0$ therefore reflects the mismatch between the actual and nominal $h\nu$, and is applied as a calibration

correction.

For example, in this work the time-resolved spectra are taken at 650 eV nominal photon energy. The Fermi edge of the Pd sample is measured at 650 eV under steady-state conditions and fitted with a complementary error function (Figure 7). The fitted edge appears at 0.55 eV instead of 0 eV, and this 0.55 eV offset is applied as a constant correction to all spectra.

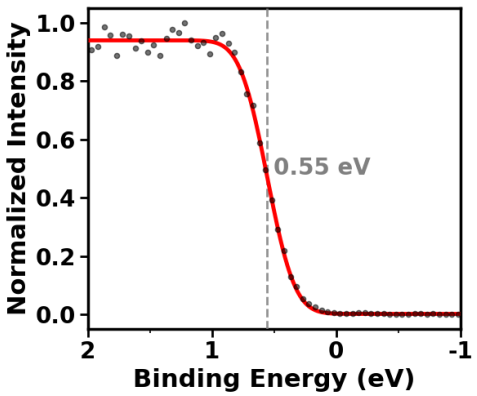

Figure 7: Fermi edge measurement of the Pd sample. The grey points are the measured data, and the red line is a complementary error function fit. The fitted center is offset by 0.55 eV from the expected $BE = 0$.

3.4 Shirley Background Subtraction

A photoelectron spectrum contains not only the peaks from core-level photoemission but also a background from secondary electrons, that is, photoelectrons that have been inelastically scattered before leaving the sample. These electrons lose part of their kinetic energy, so they appear at higher binding energies than the original peak. They accumulate on the high binding energy side, raising the baseline above that on the low binding energy side. To extract the true peak intensities, this background must be subtracted. One common method is Shirley subtraction. Compared with a polynomial fit, only the low-energy endpoint E_{low} and the integration window need to be set, and the method assumes that the spectrum is flat at both endpoints.

Shirley proposed that the background signal at a given binding energy is proportional to the total peak area at lower binding energies [17]. This can be written as:

$$\frac{dB(E)}{dE} = k \cdot P(E) \tag{11}$$

where $B(E)$ is the background, $P(E)$ is the peak signal, and k is a constant. Integrating from the low binding energy endpoint E_{low} to a given energy E:

$$B(E) = B(E_{\text{low}}) + k \int_{E_{\text{low}}}^{E} [I(E') - B(E')]\, dE' \tag{12}$$

where $I(E)$ is the measured spectrum. The integration starts from the low binding energy side because secondary electrons can only appear at higher binding energies.

Both $B(E)$ and k are unknown, so the equation is solved iteratively [18]. Figure 8 shows this process applied to the Pd 3d spectrum. The process starts with an initial guess B_0 (Initial, pink), a straight line connecting the average intensities at two endpoints, which appears curved due to the logarithmic intensity scale. The coefficient k is then determined by evaluating the integral over the full binding energy range:

$$k_n = \frac{B_{n-1}(E_{\text{high}}) - B_{n-1}(E_{\text{low}})}{\int_{E_{\text{low}}}^{E_{\text{high}}} [I(E') - B_{n-1}(E')]\, dE'} \tag{13}$$

Substituting k_n back gives B_n:

$$B_n(E) = B_{n-1}(E_{\text{low}}) + k_n \int_{E_{\text{low}}}^{E} [I(E') - B_{n-1}(E')]\, dE' \tag{14}$$

After the first (1st, orange) and second (2nd, green) iterations, the background approaches convergence. The iteration is repeated until B_n and B_{n-1} differ by less than a chosen tolerance, here 10^{-6}, giving the final converged background (Final, blue). After subtraction of the converged background, the remaining spectrum contains only the peak signal, and the peak areas can be used to compare the relative abundance of different chemical species.

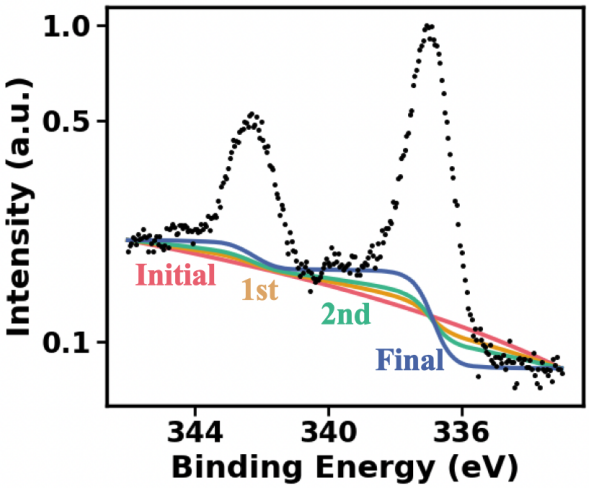

Figure 8: Iterative calculation of the Shirley background applied to the Pd 3d spectrum. The background approaches convergence after a few iterations, ultimately isolating the true peak signal.

3.5 Event Averaging

As discussed in Section 2.7, the short acquisition time per spectrum in time-resolved APXPS results in low signal intensity and a poor signal-to-noise ratio. To address this, event averaging is applied over 120 modulation cycles following the approach described by Knudsen et al. [6] and

Eads et al. [7]. A function generator drives both the NH_3 pulse valve and the data acquisition trigger, so that each cycle is exactly aligned. Figure 9 compares the O 1s region from a single cycle (a, b) and after event averaging over 120 cycles (c, d). The spectral features are significantly enhanced after averaging. The single-cycle intensity in (a, b) is rescaled for visibility.

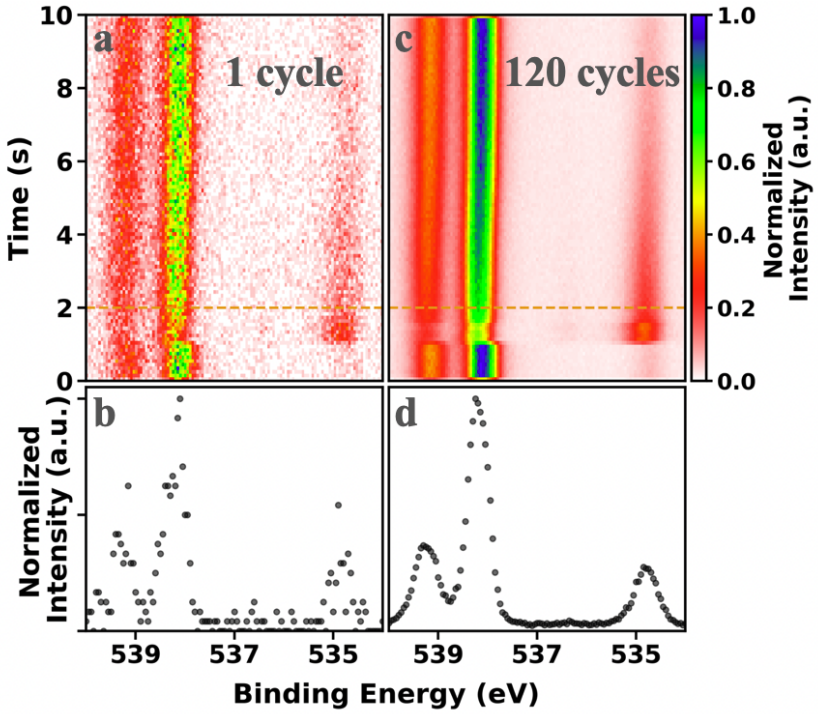

Figure 9: Comparison of the O 1s region from a single cycle (a, b) and after event averaging over 120 cycles (c, d). The single-cycle intensity is rescaled for visibility.

3.6 Peak Fitting

After the preceding corrections, each spectrum is background-subtracted, and averaged over 120 cycles and is ready for peak fitting. To obtain the intensity of each chemical component, every peak is fitted with a suitable line shape. A core-level photoemission peak is broadened by two contributions: the Gaussian broadening from the instrumental resolution, and the Lorentzian broadening from the finite core-hole lifetime. The true line shape is therefore the convolution of a Gaussian and a Lorentzian, which is a Voigt function. However, the Voigt function has no closed form, and fitting with the two broadening widths as independent parameters is often numerically unstable. Every peak is therefore fitted with a pseudo-Voigt function instead, which approximates the Voigt function and is the standard choice in XPS peak fitting.

Each peak in the spectrum is described by one pseudo-Voigt function, and their sum forms the model curve. Initial guesses for the peak positions are provided manually, and the model curve is then fitted to the measured spectrum by non-linear least squares. This procedure is repeated for every time-resolved snapshot.

3.7 Stoichiometric Intensity Rescaling

To enable a direct comparison of the abundances of O-containing and N-containing species, the intensities of the O 1s and N 1s spectra have to be rescaled to a common scale. In photoemission, the peak area reflects the abundance of the emitting species, but it also depends on the photoionization cross-section. The cross-section differs strongly between elements, so the raw peak areas from different elements cannot be compared directly.

Before the rescaling factor is determined, the fitted peak areas are first converted to represent molecular abundance. For example, one O_2 molecule contains two oxygen atoms and therefore contributes twice to the O 1s peak area, so its fitted area has to be divided by 2 to represent the number of O_2 molecules. The same division applies to N_2 and N_2O in the N 1s spectrum, while NO, NH_3, and H_2O are left unchanged. After this step, the peak areas within the O 1s spectrum and within the N 1s spectrum are separately proportional to the molecular abundances of the corresponding species. However, the two spectra still cannot be compared to each other because of the cross-section mismatch.

The rescaling factor is determined from the stoichiometry of the reactions introduced in Section 2.1.1, in which 4 NH_3 react with O_2 to produce N_2, N_2O, or NO, with H_2O produced in all three cases. Every H atom in the products comes from NH_3 and ends up in H_2O, and every N atom in the products also comes from NH_3. One N_2 or N_2O molecule is therefore accompanied by 3 H_2O, and one NO by 1.5 H_2O. Using the N-product abundances from the N 1s spectrum, the expected change in H_2O is

$$\Delta I^{\text{theo}}_{\text{H}_2\text{O}} = 3.0\Delta I_{\text{N}_2} + 3.0\Delta I_{\text{N}_2\text{O}} + 1.5\Delta I_{\text{NO}} \tag{15}$$

The rescaling factor is a single constant and can be evaluated at any time point during the NH_3 pulse, when the dose arrives in the chamber and the products are generated. Here, one such snapshot is used. Before the pulse, the chamber still contains residual reaction products from the previous cycle that have not been fully pumped away. ΔI for each species is therefore defined as the increase in its peak area in this snapshot relative to its own pre-pulse baseline. The rescaling factor is then defined as

$$s = \frac{\Delta I^{\text{theo}}_{\text{H}_2\text{O}}}{\Delta I^{\text{raw}}_{\text{H}_2\text{O}}} \tag{16}$$

and applied to every peak area in the O 1s gas-phase spectrum. After this step, the O 1s and N 1s peak areas can be compared directly as molecular abundances.

4 Ammonia Oxidation on Pd Catalyst

4.1 Experiment Setup

The experiment was performed at the HIPPIE beamline of the MAX IV synchrotron, using the solid-gas ambient-pressure X-ray photoelectron spectroscopy (APXPS) endstation. The polycrystalline Pd sample was cleaned by Ar^+ sputtering (1 kV, 10 mA, 1×10^{-5} mbar Ar, 20 min) followed by annealing at 600°C for 2 min. Surface cleanliness was verified by an XPS survey scan prior to each measurement series.

The chamber was held at 1 mbar with a continuous O_2 flow of 10 sccm. The sample was heated by a 1080 nm continuous-wave infrared laser, and measurements were carried out at two temperatures, 500 °C and 600°C. Both temperatures were measured on the same day under otherwise identical conditions.

NH_3 was introduced in a 10-second cycle with a 0.5-second pulse delivered through a solenoid valve using a flow of 1 sccm behind the valve. The reaction was probed in two measurement positions, illustrated in Figure 10. In the gas-phase position, the sample was moved away from the nozzle so that the probed volume lies between the nozzle exit and the analyzer aperture; the signal is dominated by the gas phase above the surface. In the surface-sensitive position, the sample was placed close to the nozzle so that the probed volume intersects the surface; the signal contains contributions from both the surface and the gas phase immediately above it. At each temperature, the N 1s and O 1s regions were recorded in the gas-phase position, and the O 1s, N 1s, and Pd 3d regions were recorded in the surface-sensitive position, all at a photon energy of $h\nu = 650$ eV. Each spectrum was averaged over 120 cycles following the event-averaging procedure described in Section 3.5.

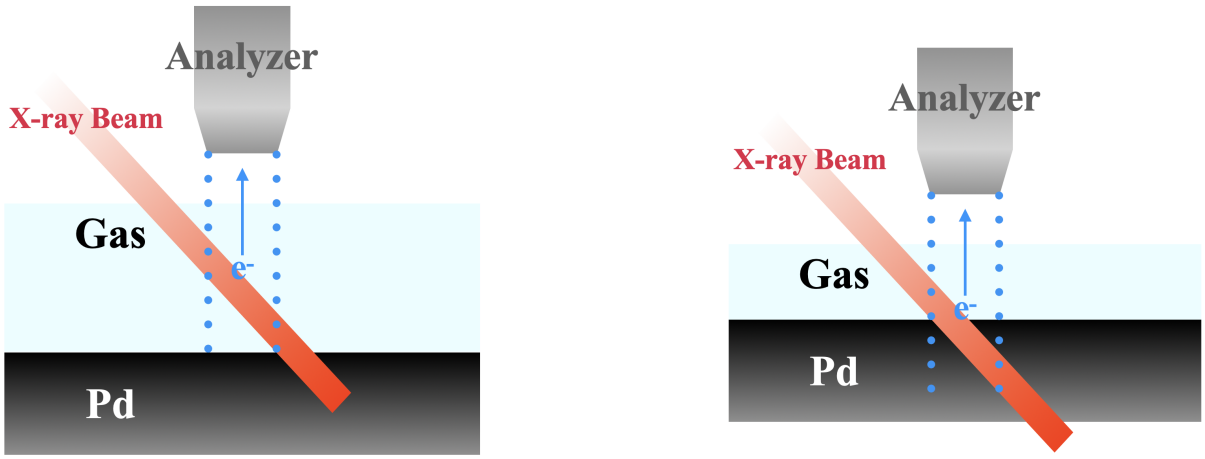

(a) Gas-phase position

(b) Surface-sensitive position

Figure 10: Experimental position for (a) gas-phase and (b) surface-sensitive measurements. In the gas-phase position, the sample is retracted from the nozzle so that the probed volume lies between the nozzle exit and the analyzer aperture. In the surface-sensitive position, the sample is placed close to the nozzle so that the probed volume intersects the surface.

4.2 Gas-Phase Spectra

We first show what the gas phase looks like during one pulse cycle at 500°C (Figure 11) and identify the reactants and products by their O 1s and N 1s binding energies. We then compare the product distributions at 500°C and 600°C (Figure 12).

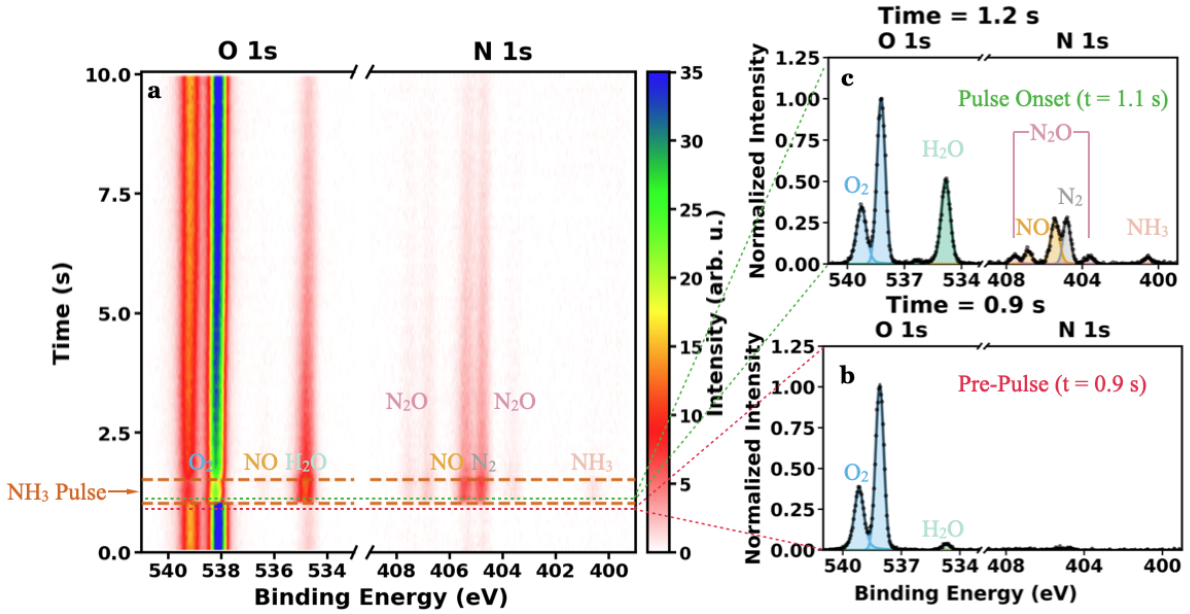

Figure 11: Time-resolved O 1s and N 1s gas-phase photoelectron spectra during the ammonia oxidation cycle at 500°C. (a) 2D intensity heat map over a 10 s cycle. The two orange dashed lines mark the 0.5 s NH_3 pulse starting at t = 1.0 s and ending at 1.5 s; the 0 to 1.0 s period belongs to the previous cycle. (b) Pre-pulse snapshot spectrum (t = 0.9 s, red dashed line), showing mostly O_2 and residual H_2O. (c) Pulse onset snapshot spectrum (t = 1.2 s, green dashed line), showing unreacted NH_3 and the new nitrogen products N_2, N_2O, and NO.

Figure 11a displays the time-resolved O 1s and N 1s gas-phase XP spectra over one full 10 s reaction cycle at 500°C. The 2D map reveals how the gas-phase composition above the Pd surface evolves as the NH_3 pulse arrives and reacts, with the two orange dashed lines marking the 0.5 s pulse window. Within the pulse window, the O_2 signal drops while H_2O grows, and several new peaks appear in the N 1s region; all features relax back to their pre-pulse state after the pulse ends.

Figures 11b and 11c are single-time snapshots, normalized individually for visual clarity. In the pre-pulse spectrum (Figure 11b, t = 0.9 s), the chamber is dominated by O_2, with a minor residual H_2O component, since water sticks strongly to the chamber walls and is hard to pump out completely. In the pulse-onset spectrum (Figure 11c, t = 1.2 s), in addition to the O_2 and H_2O features already present in (b), four new peaks appear in the N 1s region.

Following [5, 15, 19, 20], we identify the peaks in Figure 11c by their binding energies; the same color scheme is reused in Figure 12. In the N 1s region: 400.6 eV (orange) is unreacted NH_3; 404.8 eV (grey) is N_2; the multiplet at 405.3 and 406.8 eV (yellow) is NO, where exchange splitting produces a triplet and a singlet; and the two peaks at 407.5 and 403.5 eV (pink) are the

two chemically inequivalent N atoms of N_2O. In the O 1s region, the multiplet (blue) is O_2, also exchange-split, and the single feature at lower binding energy (green) is H_2O.

An analogous dataset was acquired at 600°C and processed in the same way. The corresponding 600°C dataset is shown in Figure S1.

Having identified the species at 500°C, we now compare the product distributions between 500°C and 600°C. Figure 12 shows the fitted O 1s and N 1s spectra at $t = 1.2$ s for 500°C (upper panels) and 600°C (lower panels), using the same color-to-species mapping as in Figure 11c. The $t = 1.2$ s timepoint is chosen because it lies shortly after pulse onset, when the product peaks are fully developed and the components are most cleanly resolved by the fit.

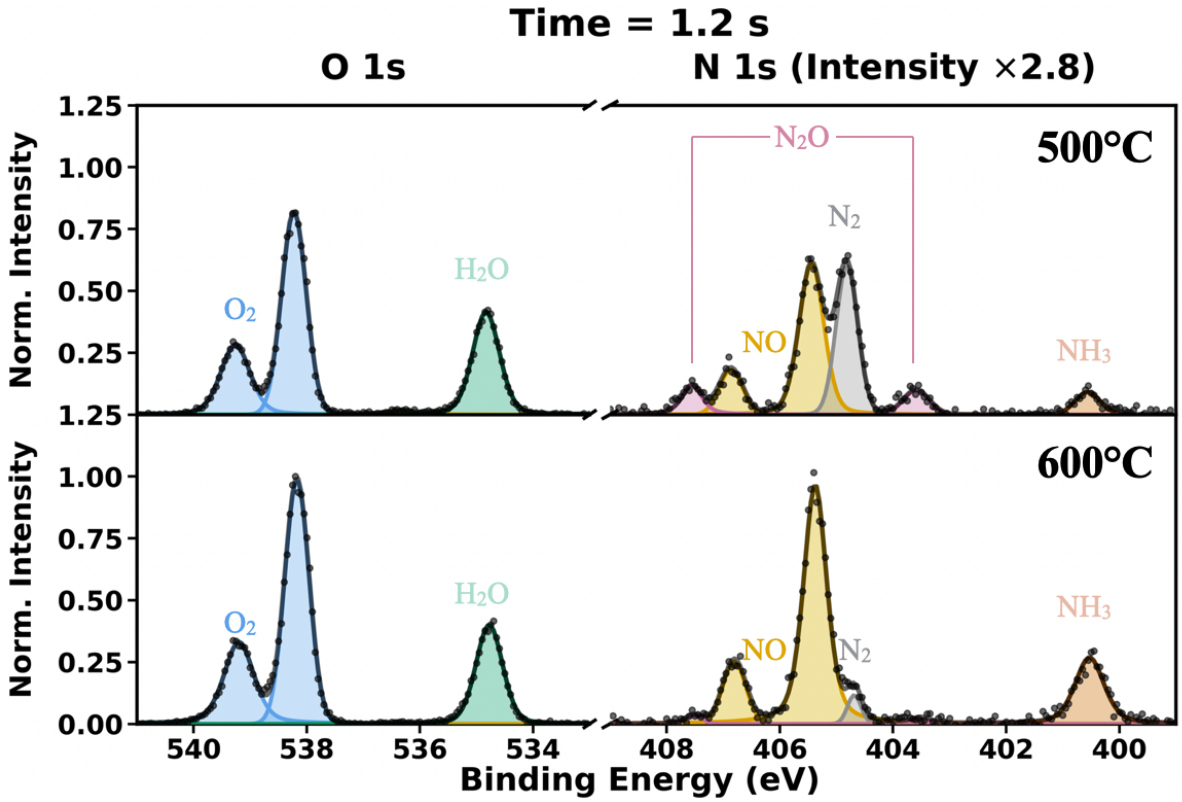

Figure 12: O 1s and N 1s gas-phase spectra during the NH_3 pulse ($t = 1.2$ s) at 500°C (upper) and 600°C (lower). The colored areas represent the components for both unreacted gases (O_2, NH_3) and reaction products (H_2O, N_2, N_2O, NO). For visual clarity, the N 1s spectral intensities are multiplied by a factor of 2.8.

The peak areas in Figure 12 from both temperatures are processed through the same two steps: curve fitting of each spectrum (Section 3.6), followed by stoichiometric rescaling between the O 1s and N 1s gas-phase spectra (Section 3.7) so that O-containing and N-containing species share a common molecular scale. Both temperatures are processed identically, which makes their product distributions directly comparable.

The product distributions differ strongly between the two temperatures, as summarized in Table 1. In the upper panels (500°C), all three nitrogen products appear, with NO the largest at 46%, while N_2 (34%) and N_2O (14%) also contribute substantially. In the lower

Table 1: Gas-phase composition of nitrogen-containing species at $t = 1.2$ s for 500°C and 600°C.

	NH_3	NO	N_2	N_2O
500°C	6%	46%	34%	14%
600°C	20%	73%	5%	2%

panels (600°C), the distribution shifts strongly toward NO (73%), and N_2 (5%) and N_2O (2%) almost disappear. More NH_3 also remains in the lower panels (20% versus 6%), indicating less NH_3 consumption at 600°C. In the O 1s region of both panels, a substantial O_2 signal remains alongside the products, so the consumption of O_2 during the pulse is only partial. This temperature-dependent change in the proportion of nitrogen products is the selectivity shift in NH_3 oxidation.

Having presented the gas-phase products, we now turn to the surface spectra, where the reaction itself takes place.

4.3 Surface Spectra

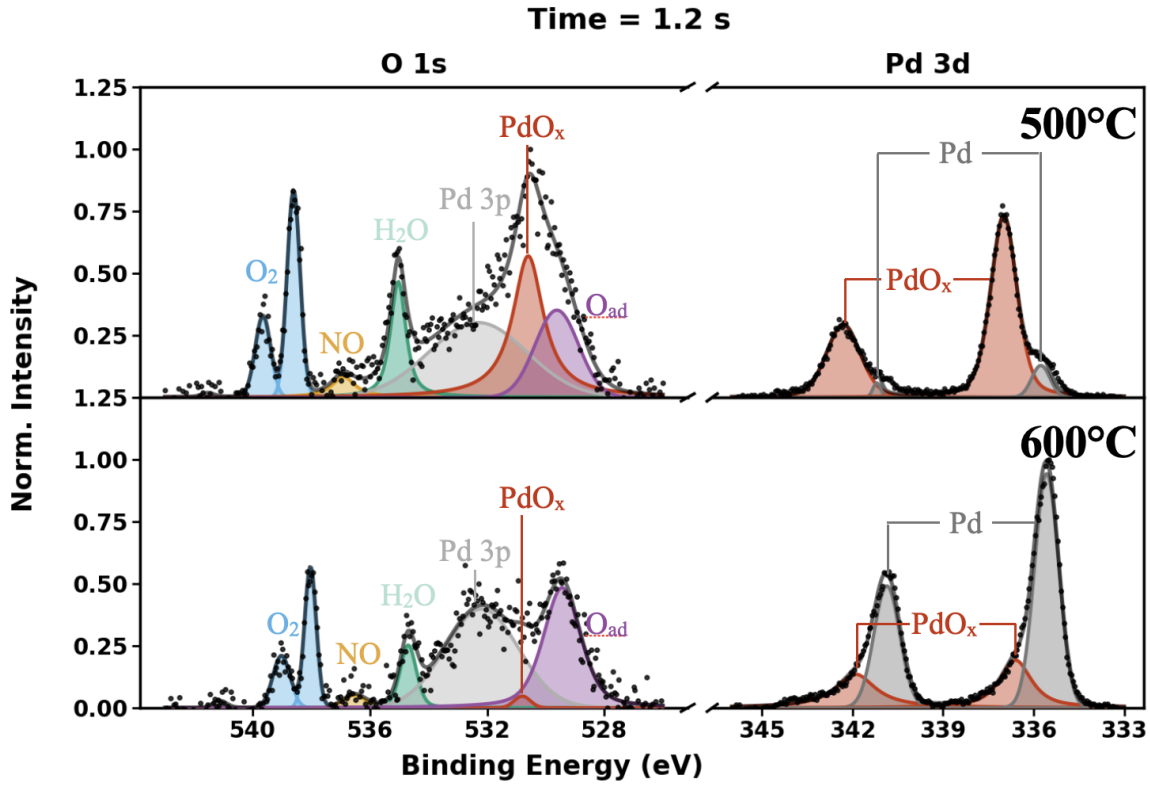

Figure 13: O 1s and Pd 3d surface spectra right after the NH_3 gas pulse arrived ($t = 1.2$ s) at 500°C and 600°C.

To compare the surface chemistry at the two temperatures, Figure 13 shows the O 1s and Pd 3d surface spectra at $t = 1.2$ s, immediately after the NH_3 gas pulse arrived, at 500°C and

600°C. Even with the surface-sensitive measurement geometry (Figure 10b), a small residual contribution from the gas phase remains.

In the higher binding energy region of the O 1s spectrum, three components are gas-phase species already assigned in Figure 12: O_2 (blue multiplet), NO (yellow), and H_2O (green). The remaining components are surface-specific. According to [6, 21], the grey peak is the Pd 3p line, the red peak is oxygen in Pd oxide, and the purple peak is surface-adsorbed oxygen.

For the Pd 3d spectra, the dark grey peaks are from metallic Pd, with the 340 eV peak from $3d_{3/2}$ and the 335 eV peak from $3d_{5/2}$ [21–23]. This splitting is due to spin-orbit coupling [24]. The red peaks in the Pd 3d spectra are Pd in Pd oxide, which also split due to spin-orbit coupling.

However, the N 1s surface spectra do not show any clear peaks (Figure S2). N-containing intermediates have a short residence time on the surface, resulting in a low average coverage below the detection limit. Consequently, the N 1s surface spectra are not discussed further.

Comparing the 500°C and 600°C results, the surface composition differs clearly between the two temperatures. At 500°C, more Pd oxide is observed in both the O 1s and Pd 3d surface spectra. At 600°C, the Pd 3d signal is dominated by metallic Pd, indicating fewer surface O atoms. This is consistent with the O 1s surface spectra, where the Pd oxide signals almost disappear. This surface picture is counterintuitive when set against the gas-phase observations in Section 4.2. At 500°C the surface holds abundant O, yet a substantial fraction of the nitrogen products is N_2, which carries no O atom; at 600°C the surface is O-depleted, yet the selectivity shifts to NO, the most O-consuming pathway. The selectivity therefore cannot be set by surface O abundance alone, and we return to this puzzle in Section 4.4.2. The same surface-state difference also bears on the NH_3 conversion at the two temperatures, which we discuss in Section 4.4.3.

4.4 Linking Surface Dynamics to Catalytic Performance

4.4.1 Surface Reaction Dynamics

Figure 14 presents the time-resolved dynamics of the gas-phase species (upper panels), and surface species (middle panels) along with the NO binding energy shifts (bottom panels). The grey shaded area indicates the NH_3 gas pulse duration at t = 1.0–1.5 s. The signals for O_2, H_2O, and surface O_{ad} are plotted on the right y-axes because their intensity scales differ substantially from the other species.

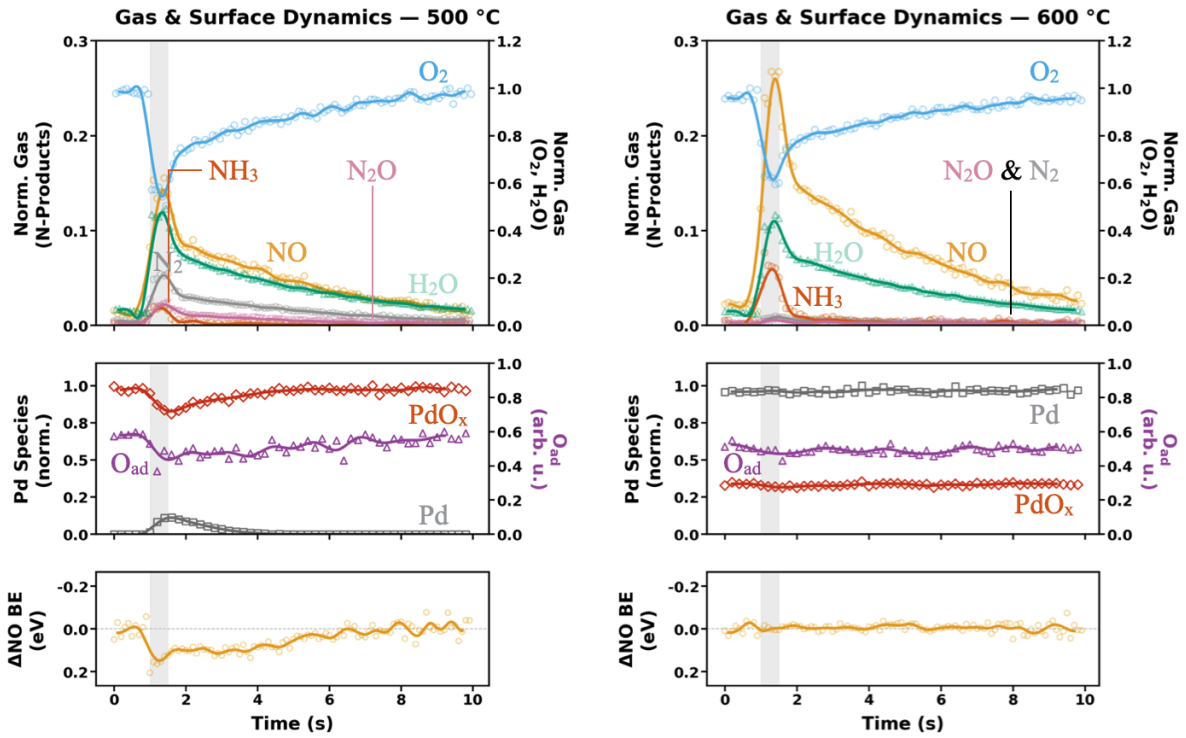

Figure 14: Time-resolved dynamics of the gas-phase species, surface species, and NO binding energy shifts at 500°C and 600°C.

In the gas phase, the arrival of the NH_3 pulse leads to a partial consumption of O_2, while H_2O and other N-containing products increase. It is important to note that O_2 is never fully depleted; a significant signal persists throughout the pulse. After the pulse, O_2 starts to recover, and the products gradually decrease to zero. Consistent with our earlier discussion on selectivity, the main difference between the two temperatures is the product distribution, where 600°C shows a significantly higher production of NO with almost no N_2 and N_2O. The mechanism behind this temperature-dependent selectivity is discussed in Section 4.4.2.

Regarding the surface species, the two temperatures exhibit distinct behavior. At 500°C, the Pd 3d signal is dominated by the oxidized component (PdO_x). Given that the photoelectron probing depth at our kinetic energy ($\sim$ 315 eV) corresponds to only a few atomic layers (Section 2.2), the dominance of the PdO_x signal indicates that the majority of the surface Pd atoms are in an oxidized state. During the NH_3 pulse, the Pd oxide and adsorbed O signals decrease, and the metallic Pd signals increase. This transient surface reduction demonstrates that the rate of surface oxygen consumption by the NH_3 pulse temporarily exceeds the rate of re-oxidation from the gas-phase O_2 supply.

The NO gas-phase binding energy provides independent confirmation of this surface reduction. As discussed in Section 2.5, this temporary surface reduction (from PdO_x to Pd) alters the surface work function, which subsequently causes the NO binding energy to shift to a higher value. At 600°C, no such shift is observed, consistent with the absence of any transient surface change.

In contrast, at 600°C, the Pd oxide signal is much weaker and Pd metal signal dominates, as the higher temperature makes PdO_x less stable. Interestingly, the signals for Pd oxide, adsorbed O, and Pd metal show no obvious changes even during the ammonia pulse. This indicates that, unlike at 500°C, the consumption and recovery of surface oxygen are balanced on a time scale faster than our measurement resolution.

Beyond the surface response, the gas-phase oxygen balance also differs between the two temperatures. Figure 15 shows the time-resolved total number of O atoms in the gas-phase products (purple), and the O_2 reactant (blue) at 500°C (upper panel) and 600°C (lower panel). The brown line represents the total number of gas-phase O atoms (O_2 + products), and the grey shaded area indicates the NH_3 pulse duration.

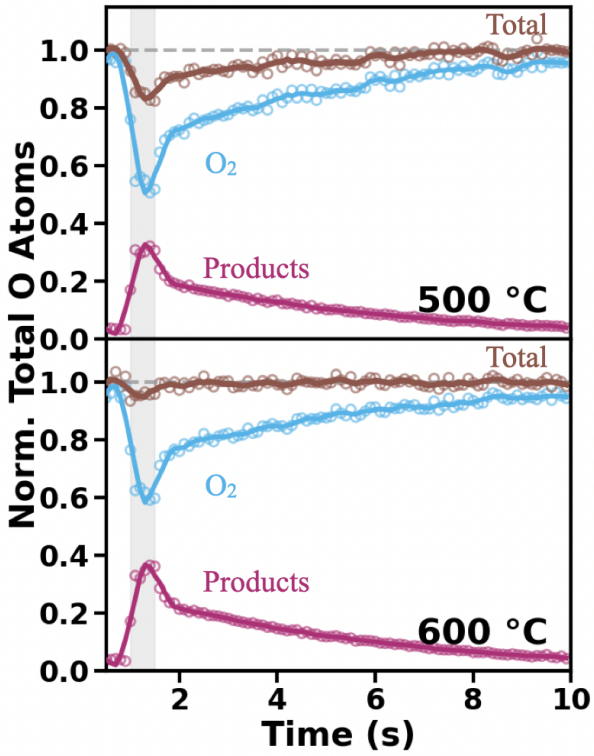

Figure 15: Time-resolved total number of O atoms in the gas phase at 500°C (upper) and 600°C (lower), separated into the O_2 reactant (blue), the products (purple), and their sum (brown). The grey shaded area marks the NH_3 pulse.

As expected, the arrival of the NH_3 pulse leads to an increase in products and a concurrent decrease in O_2. However, we observe a pronounced dip in the total O signal at 500°C, indicating an obvious loss of oxygen atoms. This "missing" oxygen is not caused by surface oxygen accumulation, as our earlier discussion in Section 4.3 confirmed that surface oxygen actually decreases at this temperature.

The difference between the two temperatures reflects which N-containing products form. At 500°C, a substantial fraction of the reacted NH_3 goes to N_2 (Table 1), which carries no O atoms. The N_2 produced replaces and dilutes the unreacted O_2, producing the visible dip in the

total O signal during the pulse. At 600°C, the selectivity shifts almost entirely to NO (Table 1); each NO produced carries an O atom from the consumed O_2, so the dilution of O_2 is much weaker, and the total O signal stays nearly flat through the pulse.

The pathway difference identified above relies on the selectivity shift toward NO at higher temperature; Section 4.4.2 examines the mechanism behind this shift.

4.4.2 Product Selectivity and NO Formation

We now turn to the mechanism behind the selectivity shift toward NO at higher temperature, comparing our observations with earlier NH_3 oxidation studies on other metal catalysts. As discussed in Section 4.3, the N 1s surface spectra show no detectable nitrogen signal at either temperature (Figure S2), indicating that surface N intermediates have a very short residence time. According to the operando APXPS study by Ivashenko et al. [5] on Pt(111) and PtRh/Pt(111) surfaces, this residence time shortens further at higher temperature, driving the selectivity toward NO. If the same picture holds for our Pd polycrystal: at 600°C, atomic N from NH_3 dehydrogenation reacts immediately with surface O to form NO, leaving little time for N–N recombination. At 500°C, the longer residence time allows N–N recombination to N_2, and the coexistence of adsorbed N and NO leads to N_2O.

We also note that even at 600°C, where the Pd oxide signals almost disappear in both the O 1s and Pd 3d spectra, NO remains the dominant product. The O 1s surface spectra still show surface-adsorbed oxygen (O_{ad}) at this temperature (Figure 14, middle panels), so NO formation does not require a bulk oxide phase. This is consistent with the same study by Ivashenko et al. [5], who showed that O_2-rich conditions consistently lead to NO production regardless of whether oxygen is present as chemisorbed atoms or within a surface oxide. Our Pd polycrystal observations align with this picture: surface O_{ad} is sufficient for NO formation, without requiring a bulk Pd oxide layer. Together with the residence-time mechanism above, this surface picture would account for the selectivity shift toward NO at higher temperature. Section 4.4.3 returns to this shift in interpreting the NH_3 conversion drop.

4.4.3 The Drop in NH_3 Conversion at Higher Temperature

So far we have seen that the surface differs in chemistry (Section 4.3) and dynamics (Section 4.4.1) between the two temperatures, and that the gas-phase product distribution shifts toward NO at the higher temperature (Section 4.2, Table 1). Table 1 also shows that the unreacted NH_3 fraction rises with temperature, corresponding to a drop in NH_3 conversion summarized in Table 2.

The NH_3 conversion drops from 94% at 500°C to 80% at 600°C. This goes against the Arrhenius expectation (Eq. (1)) that higher temperature accelerates the reaction. NH_3 oxidation consumes oxygen, so a drop in NH_3 conversion would normally be accompanied by a drop in oxygen consumption. Figure 16 shows the time-resolved O conversion at 500°C and 600°C,

Table 2: NH_3 conversion at t = 1.2 s, defined as the fraction of injected NH_3 that has reacted.

	NH_3 conversion
500°C	94%
600°C	80%

defined as the fraction of available O atoms found in the products. The two curves closely overlap, both peaking at around 40%.

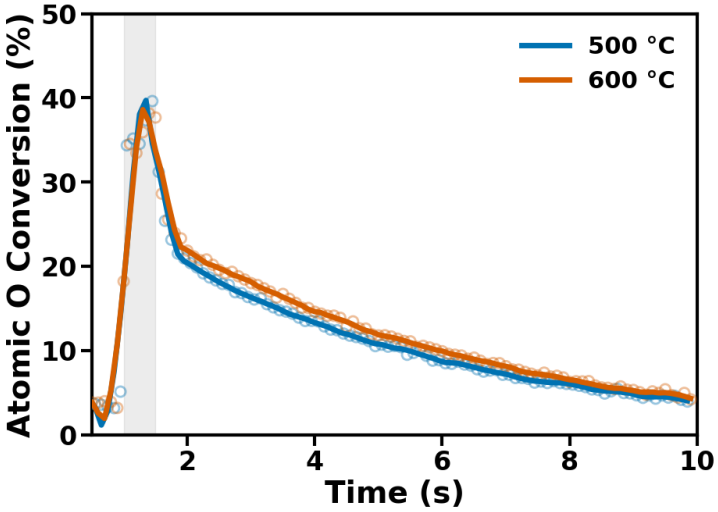

Figure 16: Time-resolved O conversion at 500°C and 600°C, calculated as the ratio of oxygen atoms in the products (purple line, Figure 15) to the total available oxygen atoms (brown line).

One reading of this match is that a single shared constraint limits O turnover at both temperatures. The most natural candidate, a mass-transfer limitation of O_2, can be ruled out from the data: gas-phase O_2 is not fully consumed during the pulse (Figure 14, upper panels) and surface oxygen also persists (Figure 14, middle panels), so the catalyst is never starved of oxygen. Other forms of shared constraint cannot be excluded with only two temperature points, but the mechanism behind any such constraint remains unclear.

We propose instead that this pattern arises from the arithmetic combination of two independent surface-driven effects. The first concerns the NH_3 conversion itself. As established in Section 4.3, the surface is dominated by Pd oxide at 500°C and is largely metallic at 600°C. Baerns et al. [2] showed by DFT calculations on Pt that adsorbed O and OH species significantly lower the activation barriers for NH_3 dehydrogenation (Section 2.1.1). If a similar relation holds for Pd, the higher surface O coverage at 500°C provides more catalytic assistance for NH_3 dehydrogenation than the metallic surface at 600°C, plausibly accounting for the higher NH_3 conversion at the lower temperature.

The second effect concerns the selectivity. As summarized in Table 1, the product distribution shifts strongly toward NO at 600°C, which is the most O-expensive of the three nitrogen products. From the reaction stoichiometries (Eqs. (2)–(4)), forming NO consumes 2.5 O atoms

per NH_3, compared with 1.5 for N_2 and 2.0 for N_2O. The observed shift toward NO therefore raises the average O cost per reacted NH_3.

In summary, the lower NH_3 conversion at 600°C and the higher per-NH_3 O cost act in opposite directions, and their combination happens to yield the same total O consumed at both temperatures. The matching $\sim$ 40% O conversion across the two temperatures is therefore a numerical coincidence between two independent temperature-driven surface effects, each with a mechanism grounded in earlier work cited in Section 2.1.1, rather than the signature of a shared O-side limit on the catalyst. Measurements at additional temperatures may help discriminate between this two-effect picture and the alternative shared-constraint reading.

4.5 Comparison with Steady-State Literature

Before comparing our results (developed in Sections 4.4.1–4.4.3) with the literature, it is essential to note a fundamental difference in experimental design. The studies discussed below [2–5] were all conducted under steady-state or quasi-steady-state conditions, in which the catalyst surface equilibrates with a constant gas mixture. In contrast, our experiment is dynamic: we start from an oxygen-covered Pd surface with no nitrogen present, inject a short NH_3 pulse, and observe the transient response. The surface state evolves continuously throughout the NH_3 pulse, so the product distribution may differ from what would form under steady-state conditions. In particular, the pulsed delivery produces transient conditions absent under continuous gas flow, such as a momentarily high NH_3 concentration near the surface and a temporarily reduced surface at 500°C (Section 4.4.1). Our experiments were conducted at 500°C and 600°C, corresponding to approximately 773 K and 873 K.

Despite the differences in experimental approach, the literature converges on a unifying principle: the product selectivity in ammonia oxidation is governed by the relative surface populations of N and O species. Weststrate et al. [4] demonstrated this most clearly on Pt(410): when the surface is covered by NH_x and atomic N species, the main product is N_2; when the surface transitions to an O-covered state, the selectivity shifts to NO; and N_2O forms only when adsorbed N and NO coexist. The same trend holds across different catalysts and pressure regimes. Baerns et al. [2] found that N_2 dominates below $\sim$ 600 K and NO at higher temperatures on Pt(533), Pt foil, and knitted Pt gauze (woven wire mesh used in industrial reactors), spanning pressures from 10^{-5} mbar to 1 bar, with higher O_2/NH_3 ratios shifting the transition to lower temperatures. Rafti et al. [3] observed on Rh(110) that a large oxygen excess (O_2:NH_3 = 10:1) strongly suppressed N_2 production and reduced the overall catalytic activity. Ivashenko et al. [5] argued that N_2 formation requires a sufficient surface N coverage. Below this, N atoms predominantly encounter O atoms and desorb as NO.

In O_2-rich environments, the transition between N_2- and NO-dominated regimes has been reported between roughly 450 K and 600 K, depending on the catalyst and the O_2/NH_3 ratio. Studies on Pt(410) [4] (under 1:5 NH_3:O_2) and PtRh alloys [5] indicate transition temperatures

around 450 K and 600 K, respectively. Even below these temperature limits, the maximum reported yields for N_2 and N_2O remain relatively minor, typically not exceeding 16% and 9%.

Our experimental temperatures of 500°C and 600°C are well above all of these reported transition temperatures. Under steady-state O_2-rich conditions, N_2 and N_2O production should therefore be negligible at both temperatures. Yet at 500°C, we observe N_2 at 34% and N_2O at 14%, a combined yield of 48%, far exceeding any steady-state value reported in the literature at comparable temperatures. The product distribution approaches the expected NO-dominated regime only at 600°C.

Two factors may contribute to this elevated N_2 and N_2O production. First, the instantaneous NH_3 concentration at the catalyst surface during the pulse is likely higher than the nominal 1:10 ratio suggests, since the pulse delivers a 0.5 s burst of NH_3 into a chamber otherwise dominated by O_2. This concentrated burst of NH_3 may lead to rapid dissociation and a transient elevation in surface N coverage that, although too brief to be resolved in our N 1s spectra, could be sufficient to enable N–N recombination and N + NO association. Such conditions would not arise under the dilute, continuous-flow conditions of steady-state. Second, the polycrystalline Pd surface may possess intrinsic properties that allow N_2 and N_2O to form at higher temperatures than on Pt or Rh. Our data show a transition temperature 170–320 K above the range reported for Pt and PtRh, which suggests that Pd may provide a more favorable environment for stabilizing transient N intermediates. However, confirming this would require systematic steady-state experiments on polycrystalline Pd to separate the contributions of the pulsed experimental design from the intrinsic catalyst properties.

In summary, the selectivity of ammonia oxidation over polycrystalline Pd follows the same surface-coverage picture that the Pt and Rh literature converges on: the product distribution is controlled by the balance between surface N and O populations. What distinguishes our system is the remarkably high transition temperature and the sustained production of N_2 and N_2O at 500°C under highly oxidizing conditions, which we attribute to the combined effects of the pulsed experimental design and possible intrinsic properties of the Pd surface.

5 Conclusion and Outlook

This thesis used tr-APXPS to follow NH_3 oxidation on a polycrystalline Pd catalyst under pulsed gas conditions. The catalyst was held under a continuous O_2 flow at 1 mbar and exposed to a 0.5 s NH_3 pulse every 10 s. The cycle was repeated 120 times to enable event-averaging, and the reaction was measured at 500°C and 600°C to compare a surface that retains its oxide phase with one that is largely reduced.

Three findings emerge from these pulsed measurements. First, the surface chemistry of the Pd polycrystal differs markedly between the two temperatures. At 500°C, the surface is dominated by Pd oxide before each pulse, and the arriving NH_3 drives a transient surface reduction that is independently confirmed by a shift in the gas-phase NO binding energy. At 600°C, the surface is largely metallic, and the consumption and recovery of surface oxygen are balanced on a time scale faster than our measurement resolution.

Second, the product selectivity shifts with temperature. At 500°C, NH_3 is converted to a mixture of N_2 (34%), N_2O (14%), and NO (46%). At 600°C, the selectivity shifts almost entirely toward NO (73%), with N_2 and N_2O suppressed below 5% each. We propose that this shift follows from a shorter surface N residence time at higher temperature.

Third, the overall NH_3 conversion drops from 94% at 500°C to 80% at 600°C, while the peak oxygen conversion remains around 40% at both temperatures. We propose that the conversion drop reflects the temperature-driven change in surface O coverage: adsorbed O and OH species at 500°C provide more catalytic assistance for NH_3 dehydrogenation than the metallic surface at 600°C (Section 4.4.3). The matching $\sim$ 40% O conversion at both temperatures would then emerge as a numerical coincidence between this conversion drop and the selectivity-driven rise in per-NH_3 O cost at higher temperature.

A comparison with steady-state ammonia oxidation studies on Pt and Rh under comparable O_2-rich conditions highlights the sustained production of N_2 and N_2O at 500°C (a combined yield of 48%) as the most striking feature of our data, since this temperature is above the N_2-to-NO transitions reported in the literature. We propose that two factors may contribute. First, the residence time of surface N on Pd may be longer than on Pt or Rh, allowing more N–N recombination. Second, the pulsed delivery of NH_3 may briefly raise the surface N coverage during each pulse, enabling N–N recombination. Our two-temperature dataset cannot separate the two contributions.

A limitation of the present work is that the N 1s surface signal of nitrogen-containing intermediates remained below our detection limit at both temperatures, so the surface-side mechanisms proposed in this thesis cannot be tested directly in our data. Further work would benefit from measurements at additional temperatures, from improved N 1s sensitivity, and from a steady-state reference experiment on the same polycrystalline Pd sample. Such measurements would help test the surface-coverage and residence-time mechanisms proposed here, examine whether the matching $\sim$ 40% O conversion at the two temperatures reflects the numerical

coincidence we propose, and clarify the relative contributions of the catalyst material and the pulsed delivery to the elevated N_2 and N_2O production observed at 500°C.

Acknowledgments

I would like to thank my supervisor, Jan Knudsen, for guiding me through this project. Jan often answers my questions with questions of his own, leading me to reach the answer through my own thinking rather than simply being told. I am also grateful for the chance to take part in many interesting beamtimes over the course of this work, for his patience while I have searched for the right words in English, for the consistently positive tone of his feedback, and for the opportunity to attend the MAX IV User Meeting.

I would also like to thank my co-supervisor, Ulrike Küst. Her routine of ending every meeting with the words "good work" has been an important source of encouragement to me. I am grateful for her patience in answering my questions during beamtimes, and for the detailed and substantive feedback she has given on every thesis draft.

Many people at MAX IV have made this work possible. I thank Andrey Shavorskiy at the HIPPIE beamline for his support during beamtimes and for the feedback he gave on my poster at the MAX IV User Meeting. I thank Mihai Pop for his help with the Python data analysis, and Shah Zareen for sharing many late-night hours of beamtime with me. I am also grateful to Byungnam Ahn at the FemtoMAX beamline for answering my experimental questions and for his advice on the career questions I raised. My thanks also go to the broader HIPPIE and MAX IV staff who supported the experiments behind this work.

On the writing of this thesis, I would like to thank Jan and Ulrike for the many rounds of back-and-forth through which the text took shape. I am also grateful to Anthropic's Claude AI for its assistance with grammar review of the manuscript and with the development of the Python code used for data analysis.

Finally, I thank my partner, Min Li, who came with me to Lund for her own master's degree. She has been my steady companion through every period of self-doubt and anxiety over these two years. Congratulations on finishing your thesis as well.

Code Availability

The Python code implementing the data treatment steps described in Section 3 (transmission function correction, attenuation normalization, Fermi edge calibration, Shirley background subtraction, event averaging, peak fitting, and stoichiometric intensity rescaling) is available as a public GitHub repository: https://github.com/Hong-Ye-Lin/APXPS-Analysis-Demo.

References

[1] Jan Willem Erisman et al. “How a century of ammonia synthesis changed the world”. In: *Nature Geoscience* 1 (2008), pp. 636–639. DOI: 10.1038/ngeo325.

[2] M. Baerns et al. “Bridging the pressure and material gap in the catalytic ammonia oxidation: structural and catalytic properties of different platinum catalysts”. In: *Journal of Catalysis* 232 (2005), pp. 226–238. DOI: 10.1016/j.jcat.2005.03.002. URL: https://doi.org/10.1016/j.jcat.2005.03.002.

[3] Matías Rafti, Florian Lovis, and Ronald Imbihl. “The O2 + NH3 Reaction Over Rh(110): Steady State Kinetics and Oscillatory Behavior”. In: *Catalysis Letters* 142 (2012), pp. 16–21. DOI: 10.1007/s10562-011-0722-z. URL: https://doi.org/10.1007/s10562-011-0722-z.

[4] C. J. Weststrate et al. “Ammonia oxidation on Pt(410)”. In: *Journal of Catalysis* 242.1 (2006), pp. 184–194. DOI: 10.1016/j.jcat.2006.06.011. URL: https://doi.org/10.1016/j.jcat.2006.06.011.

[5] Oleksii Ivashenko et al. “How Surface Species Drive Product Distribution during Ammonia Oxidation: An STM and Operando APXPS Study”. In: *ACS Catalysis* 11.14 (2021), pp. 8261–8273. DOI: 10.1021/acscatal.1c00956.

[6] Jan Knudsen et al. “Stroboscopic operando spectroscopy of the dynamics in heterogeneous catalysis by event-averaging”. In: *Nature Communications* 12.1 (2021), p. 6117. DOI: 10.1038/s41467-021-26372-y. URL: https://doi.org/10.1038/s41467-021-26372-y.

[7] Calley N. Eads et al. “Resolving active species during the carbon monoxide oxidation over Pt(111) on the microsecond timescale”. In: *Nature Communications* 16 (2025), p. 1216. DOI: 10.1038/s41467-025-56576-5. URL: https://doi.org/10.1038/s41467-025-56576-5.

[8] I. Chorkendorff and J. W. Niemantsverdriet. *Concepts of Modern Catalysis and Kinetics*. Weinheim: Wiley-VCH Verlag GmbH & Co. KGaA, 2003. ISBN: 978-3-527-30574-2. DOI: 10.1002/3527602658.

[9] Ulrike Katrin Küst. “Fourier Analysis of Dynamic Catalyst Surfaces: A Time-Resolved Operando Photoemission Study of Catalytic Methane Oxidation”. Doctoral Thesis. Lund University, 2025.

[10] Albert Einstein. “Über einen die Erzeugung und Verwandlung des Lichtes betreffenden heuristischen Gesichtspunkt”. In: *Annalen der Physik* 322.6 (1905). (Nobel Prize in Physics 1921 for the photoelectric effect), pp. 132–148.

[11] Kai Siegbahn. “Electron spectroscopy for atoms, molecules, and condensed matter”. In: *Reviews of Modern Physics* 54.3 (1982). (Nobel Lecture, Nobel Prize in Physics 1981), pp. 709–728. DOI: 10.1103/RevModPhys.54.709.

[12] Niclas Johansson. “Synchrotron-based In Situ Electron Spectroscopy Applied to Oxide Formation and Catalysis”. Doctoral Thesis. Lund University, 2017.

[13] Suyun Zhu et al. “HIPPIE: a new platform for ambient-pressure X-ray photoelectron spectroscopy at the MAX IV Laboratory”. In: *Journal of Synchrotron Radiation* 28.2 (2021), pp. 624–636. DOI: 10.1107/S160057752100103X.

[14] D. Frank Ogletree et al. “A differentially pumped electrostatic lens system for photoemission studies in the millibar range”. In: *Review of Scientific Instruments* 73.11 (Nov. 2002), pp. 3872–3877. DOI: 10.1063/1.1512336. URL: https://pubs.aip.org/rsi/article/73/11/3872/456260/A-differentially-pumped-electrostatic-lens-system.

[15] Ulrike Küst et al. “Carbon subsurface traffic jam as driver for methane oxidation activity and selectivity on palladium surfaces”. In: *Nature Communications* 16 (2025), p. 7755. DOI: 10.1038/s41467-025-63088-9. URL: https://doi.org/10.1038/s41467-025-63088-9.

[16] Dieter Baurecht and Urs Peter Fringeli. “Quantitative modulated excitation Fourier transform infrared spectroscopy”. In: *Review of Scientific Instruments* 72.10 (2001), pp. 3782–3792. DOI: 10.1063/1.1400152.

[17] D. A. Shirley. “High-Resolution X-Ray Photoemission Spectrum of the Valence Bands of Gold”. en. In: *Physical Review B* 5.12 (June 1972), pp. 4709–4714. ISSN: 0556-2805. DOI: 10.1103/PhysRevB.5.4709. URL: https://link.aps.org/doi/10.1103/PhysRevB.5.4709.

[18] Alberto Herrera-Gomez. *The Peak-Shirley Background*. Internal Report. Created: 08/2011. Last Update: 02/2012. CINVESTAV-Unidad Querétaro, 2012.

[19] S. H. Overbury et al. “Chemisorption and Reaction of NO and N2O on Oxidized and Reduced Ceria Surfaces Studied by Soft X-Ray Photoemission Spectroscopy and Desorption Spectroscopy”. In: *Journal of Catalysis* 186 (1999), pp. 296–309. DOI: 10.1006/jcat.1999.2577.

[20] J. C. Fuggle and D. Menzel. “XPS, UPS and XAES studies of the adsorption of nitrogen, oxygen, and nitrogen oxides on W(110) at 300 and 100 K. I. Adsorption of N2, N2O and NO2/N2O4”. In: *Surface Science* 79 (1979), pp. 1–25. DOI: 10.1016/0039-6028(79)90022-0.

[21] Vasco R. Fernandes et al. “Reversed Hysteresis during CO Oxidation over Pd75Ag25(100)”. In: *ACS Catalysis* 6.6 (2016), pp. 4154–4161. DOI: 10.1021/acscatal.6b00658. URL: https://pubs.acs.org/doi/10.1021/acscatal.6b00658.

[22] R. Westerström et al. “Oxidation and reduction of Pd(100) and aerosol-deposited Pd nanoparticles”. In: *Physical Review B* 83.11 (2011), p. 115440. DOI: 10.1103/PhysRevB.83.115440. URL: https://doi.org/10.1103/PhysRevB.83.115440.

[23] Patrick J. Cappillino et al. “Nanoporous Pd alloys with compositionally tunable hydrogen storage properties prepared by nanoparticle consolidation”. In: *Journal of Materials Chemistry* 22.28 (2012), pp. 14013–14022. DOI: 10.1039/c2jm30988b. URL: https://doi.org/10.1039/c2jm30988b.

[24] Stefan Hüfner. *Photoelectron Spectroscopy: Principles and Applications*. 3rd. Berlin, Heidelberg: Springer-Verlag, 2003. ISBN: 978-3-662-09280-4. DOI: 10.1007/978-3-662-09280-4.

A Supplementary Information

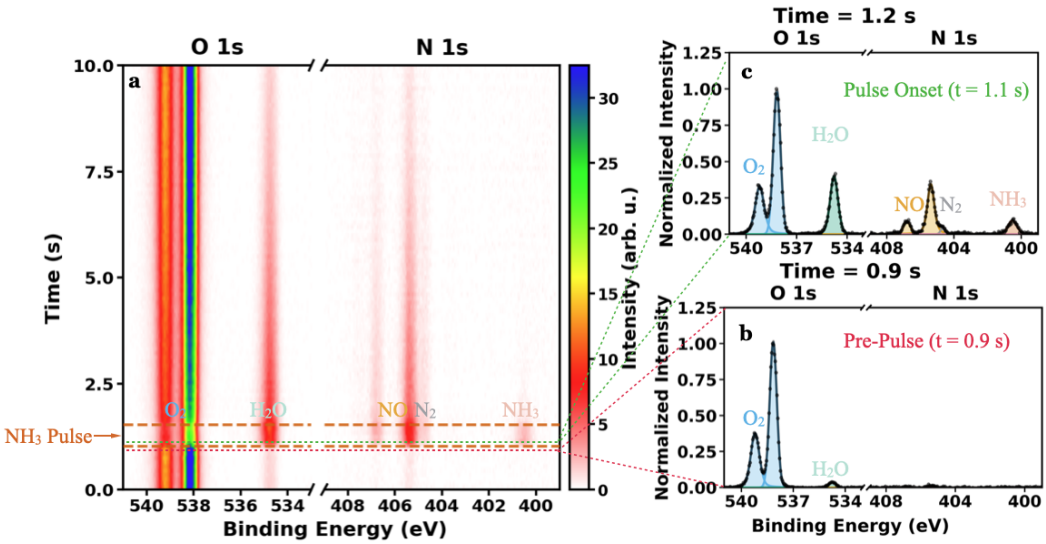

Figure S1: Time-resolved O 1s and N 1s gas-phase photoelectron spectra during the ammonia oxidation cycle at 600°C.

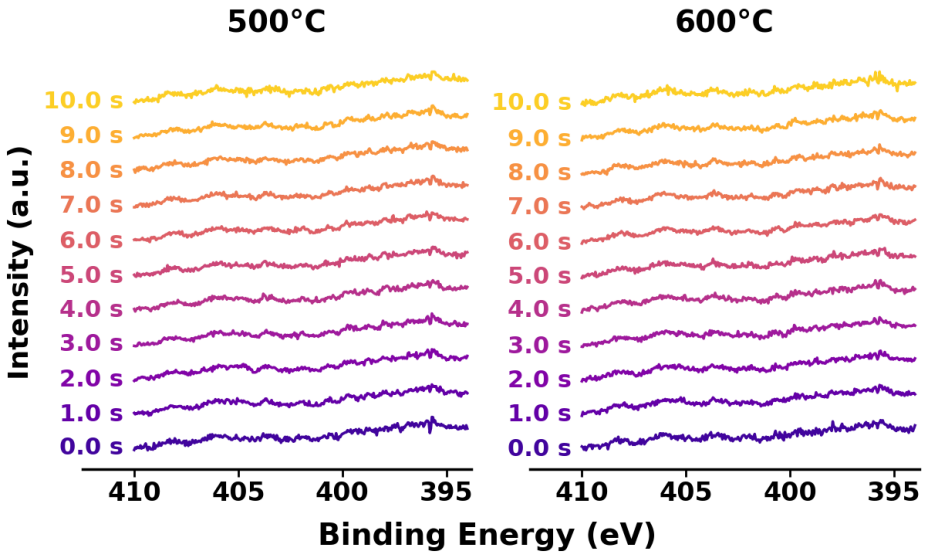

Figure S2: Waterfall plots of the N 1s surface spectra during ammonia oxidation at 500°C and 600°C. The lack of clear peaks indicates that the surface coverage of N-containing intermediates is below the detection limit.